



Aerodynamic interactions of blunt bodies free-flying in hypersonic flow

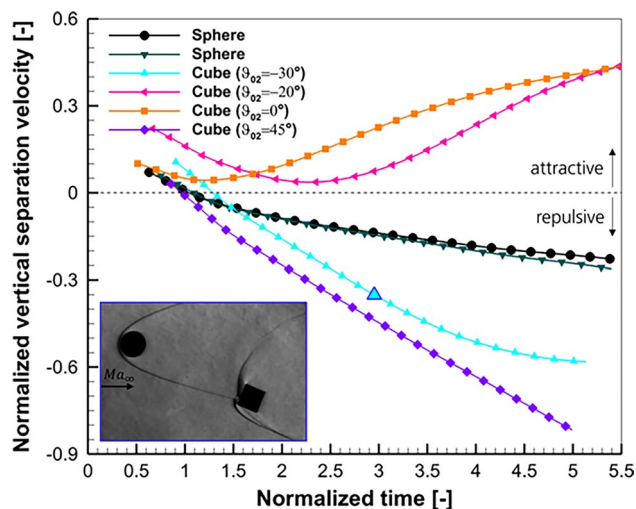
Patrick M. Seltner¹ · Sebastian Willems¹ · Ali Gülhan¹

Received: 13 September 2023 / Revised: 17 April 2024 / Accepted: 18 April 2024
© The Author(s) 2024

Abstract

This paper takes a new look at how the aerodynamic interactions of multiple bodies in high-speed flow affect their motion behaviors. The influence of the body shape and orientation on aerodynamic and stability behavior in the case of shock–shock and wake–shock interactions is the focus of this publication. Experiments were performed in the hypersonic wind tunnel H2K at the German Aerospace Center (DLR) in Cologne. Free-flight tests with tandem arrangements of spheres and cubes were performed with a synchronized dropping of both objects at various initial conditions of relative streamwise and vertical distance as well as pitch angle. A high-speed stereo-tracking captured the model motions during free-flight, and high-speed schlieren videography provided documentation of the flow topology. Based on the measured 6-degrees-of-freedom (6DoF) motion data, aerodynamic coefficients were determined. As a result, the final lateral velocity of trailing cubes is found to be many times greater than that of spheres regarding shock-wave surfing. For rotating cubes, the results showed that stable shock-wave surfing can become possible over an increasingly wide range of initial positions. This study has identified that the trailing drag coefficient of two axially aligned objects varies strongly with their relative streamwise distance. Furthermore, it was shown that the wake is a region of stability for downstream objects.

Graphical abstract



✉ Patrick M. Seltner
patrick.seltner@dlr.de

¹ Supersonic and Hypersonic Technologies Department,
Institute of Aerodynamics and Flow Technology, German
Aerospace Center (DLR), 51170 Cologne, Germany

1 Introduction

Aerodynamic interactions of multiple blunt bodies traveling at hypersonic speed play a major role in several important situations of atmospheric entry. Applications can be found for both the human-generated and natural objects. On the one

hand, (re)entry of operating, decommissioned or mission-related space objects can be attributed to human-generated situations, which also includes stage separation of launch vehicles and deorbiting of space debris, just to name a few. On the other hand, such examples as binary asteroids entering planetary atmosphere and fragmented asteroids after atmospheric breakup occur in the natural world. Estimating their flight trajectories, velocities and sizes helps to predict or, respectively, to affect the impact footprint of controlled and uncontrolled entering objects from outer space with the purpose to protect people and property from harm. In addition to the frequently studied phenomenon of shock-shock interaction (SSI), the aerodynamic interactions of fragments within the wake of another fragment moving at hypersonic speed, the so-called wake–shock interaction (WSI), have a considerable impact on the masses and velocities of trailing objects due to the aerothermodynamic shielding from heating, stress and drag (Patel et al. 2023). This phenomenon can provoke a higher momentum of grouped fragments compared to isolated ones. However, the effects occurring during atmospheric entry are so complex that state-of-the-art engineering tools are still not accurate enough to satisfactorily model these effects.

The first systematic analysis considering interaction phenomenon was made by Passey and Melosh (1980), who examined various terrestrial crater fields of past impact events and derived the well-known scaling law of the final lateral velocity v_T between the leading and trailing body of radii $r_1 \geq r_2$ based on their constant C with values in the range of 0.02 to 1.52. This equation is defined as:

$$v_T = \sqrt{\frac{3}{2} C \frac{r_1}{r_2} \frac{\rho_\infty}{\rho_m} v_\infty}, \quad (1)$$

where v_∞ is the velocity of the entering object through the atmosphere (or rather the free-stream velocity), ρ_∞ and ρ_m are the free-stream and material densities, respectively. They identified that gravity, rotation and shock-shock interaction of the fragments are the major effects on dispersion limiting merely to lateral separation in their work. However, Schultz and Sugita (1994) have shown in ballistic range tests that small fragments collimate rather than disperse, whereby they move along the bow shock of a debris cloud followed by an entrainment in the shock-bounded region of the main body. In contrast, Laurence and Deiterding (2011) found that these fragments travel along the bow shock of another upstream object due to SSI, which became known as shock-wave surfing. Such surfing behavior has been observed in several studies (Lemieux 1999; Artemieva and Shuvalov 1996, 2001; Laurence et al. 2012; Park and Brown 2012; Zhukov et al. 2013; Li et al. 2015; Park and Park 2020).

There is a vast amount of literature (Erengil et al. 1995; Artemieva and Shuvalov 1996, 2001; Zhukov et al. 2002;

Zhdan et al. 2004, 2005; Zhukov et al. 2013) on equal-sized generic blunt bodies in situations of SSI and partly in WSI. In the experiments about projectiles in tandem configurations, Erengil et al. (1995) stated that the drag of the trailing body in a near-wake is less than that of the leading one, which decreases drastically if both bodies are axially aligned with the inflow. The reason of this drag reduction was found in the surface pressure distribution of the secondary body, whereby the pressure in stagnation point is approximately 5% of the single-body value. Furthermore, a significant local pressure peak was measured slightly downstream of the stagnation point resulting from the high momentum of the wake's shear layer. Artemieva and Shuvalov (1996) carried out numerical simulations concerning the motion of two identical objects in various relative configurations and revealed a strong dependency on the aerodynamic forces in doing so. For side-by-side arrangements, high repulsive forces were noted that rapidly decrease with increasing lateral distance tending to zero. Moreover, an escape of an object from the near-wake of another was observed in their analysis. In a further study, Artemieva and Shuvalov (2001) investigated the aerodynamic interaction of up to 27 identical objects, which extends the validity of the collimation effect to a large number of fragments. Aeroballistic experiments on tandem cubes were conducted by Zhukov et al. (2002, 2013) demonstrating that both axially aligned bodies experience no change in flight attitude when the trailing body is located in the far-wake of the other ($\frac{\Delta x}{l} \approx 20$).

Many attempts have been made to study the SSI between two unequal-sized spheres of different radius ratios in proximal configurations (Laurence et al. 2007, 2009; Barri 2010; Laurence and Deiterding 2011; Laurence et al. 2012). Laurence et al. (2007) have shown a strong impact of the size ratio on the lift coefficient of a trailing body being placed downstream of a larger one. Unsteady separation behavior of freely moving spheres was subsequently analyzed in Laurence and Deiterding (2011) and Laurence et al. (2012). These studies provided evidence that the qualitative separation behavior and the final lateral velocity of secondary smaller spheres vary widely with both the radius ratio and the initial alignment angle of the two spheres. As a result, a critical radius ratio for a given initial alignment angle and vice versa a critical initial angle for a given radius ratio were determined at which the transition from entrainment to expulsion of the trailing object occurs. Secondary bodies that are axially aligned with the primary ones are entrained within the region enclosed by the primary bow shock for low radius ratios $\frac{r_2}{r_1} \leq 0.5$, whereas they are expelled from the region for high values $\frac{r_2}{r_1} \geq 0.625$ (Laurence et al. 2012). Moreover, the critical values represent the limiting cases that enables shock-wave surfing having a final lateral velocity close to maximum.

Due to the focus on spherical bodies of previous publications, subsequent researches (Li et al. 2015; Lukashenko and Maksimov 2020; Park et al. 2021) have studied other blunt geometries to enable rotational effects on the aerodynamics of two interacting objects to be investigated. For a cube lying initially next to a sphere, a similar separation behavior as in (Laurence and Deiterding 2011) and the occurrence of shock-wave surfing phenomenon on the cube were both observed by Li et al. (2015). It was found that a time extension of surfing due to the rotation occurred, which lead to a higher final lateral velocity. In addition, this effect disappears for an initial lateral distance of $\frac{\Delta z}{r} > 2.4$. By performing 2D Euler simulations, Lukashenko and Maksimov (2020) investigated side-by-side configurations of differently shaped objects applying circles, squares and rectangles. They reported as the first that the shape of the object heavily affects the separation behavior and therefore the lift force and lateral velocity, whereas the geometry of the neighboring body has no significant influence on the lateral motion. Moreover, Lukashenko and Maksimov (2020) confirmed the findings of Li et al. (2015) on extended shock-wave surfing due to the rotation effect and mentioned an increase of the lift force and final lateral velocity through higher aspect ratio of the geometry. Recently, Park et al. (2021) experimentally studied side-by-side configurations of different pairings of spheres, cubes and cylinders, whereby they found that the lateral separation is the result of both the shock-shock interaction and the lift force due to inclination. The authors also pointed out that the final lateral velocities of cylinders and cubes are nearly twice as large as of spheres.

In comparison with research discussed so far, current activities are focused on the aerodynamic interaction of multiple bodies with more than two objects (Park and Park 2020; Whalen et al. 2020; Whalen and Laurence 2021), the rarefaction effect on SSI (Cardona et al. 2021; Cardona and Lago 2022) and multi-body aerodynamics of specific problems (Leiser et al. 2022; Kovács et al. 2023). Moreover, Patel et al. (2023) discovered in their numerical analysis that a cylinder directly behind another experiences a reduction in heat transfer and surface pressure on the forebody, provoking a change in the peak heat transfer of up to -90% and a change in stagnation pressure of up to -40% related to an isolated body.

Although extensive research has been carried out on the aerodynamic interaction of spherical models, few studies examine the impact of the body shape and orientation on the motion behavior, and even less experimental data are available. In particular, it remains as open question as to how the flight attitude of a non-spherical trailing object affects its separation behavior and thus the final lateral velocity. Furthermore, it is not completely clear what factors explain the discrepancy in the maximal final lateral velocity of asteroid fragments between the analysis of real atmospheric

entry events by Passey and Melosh (1980) and recent laboratory studies. While most research has been carried out on shock-shock interaction, little attention has been paid to wake-shock interaction associated with atmospheric entry and breakup, which is important for the final kinetic energy. Previous experimental studies that have focused on wake-shock interactions have some weaknesses in their setup. One the one hand, the tests by Erengil et al. (1995) with model supports exhibit significant interference levels that lead to a lack of axial symmetry regarding the wake. On the other hand, the work of Zhukov et al. (2002, 2013) is limited to a qualitative analysis by use of schlieren photography. Finally, a systematic understanding of how the stream-wise distance between two objects influences the trailing drag coefficient is still lacking.

The purpose of this paper is to develop an understanding of the motion behavior and the flow topology during shock-shock interaction and wake-shock interaction with focus on the impact of body shape and inclination in terms of sphere-sphere (S-S), sphere-cube (S-C) and cube-cube (C-C) tandem arrangements. In addition, the question of how the body shape and inclination affect the separation behavior may address the gap between the observed strewn fields with their corresponding maximal lateral separation velocities as in (Passey and Melosh 1980) and previous scientific investigations. Experimental tests were carried out in the continuum flow regime at Mach-7 in the DLR's Hypersonic Wind Tunnel Cologne (H2K) by the use of a free-flight technique in combination with non-intrusive stereo-tracking measurement technique and high-speed schlieren videography. This article begins with describing the experimental setup and data processing in Sect. 2. It presents and discusses the results of SSI cases in Sect. 3.1 and WSI configurations in Sect. 3.2. Finally, conclusions are drawn in Sect. 4.

2 Models & methods

The experimental setup and data processing were more or less identical to that of previous works as detailed in Seltner et al. (2019). This section gives a short description of the main details with minor modifications, whereby the test facility, model release mechanism, measurement technique and post-processing system are outlined.

2.1 Hypersonic Wind Tunnel Cologne (H2K)

All experiments were performed in the Hypersonic Wind Tunnel Cologne H2K, which is located at the Supersonic and Hypersonic Technologies Department of DLR. This test facility is an intermittently working blowdown facility that comprises pressure vessels, a settling chamber, axisymmetric contoured Laval nozzles for fixed design Mach

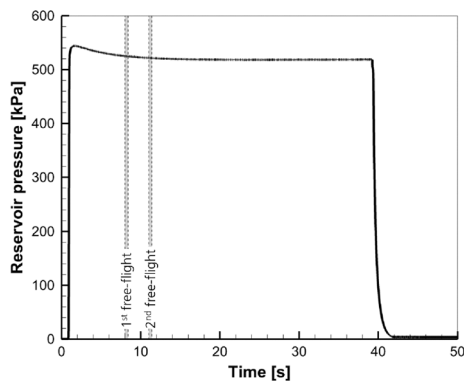


Fig. 1 Typical trace of reservoir pressure over time for complete run of H2K; dashed boxes indicate duration of free flights

numbers, a cylindrical free-jet test section with several optical accesses, a water-cooled diffuser and a vacuum sphere. At the nozzle exit, the diameter is 600 mm.

During each test, the facility operating conditions like the reservoir pressure p_0 and the reservoir temperature T_0 were measured in H2K's settling chamber with a sampling rate of 50 Hz. For the measurement of reservoir pressure, GE Druck's absolute pressure transducer of the UNIK 5000 series was applied with a total accuracy of ± 2.8 kPa for reservoir pressures between 250 kPa and 5500 kPa. An example of a reservoir pressure trace is shown in Fig. 1, where the total time of steady flow is more than 30 s after a short start-up period. For the measurement of reservoir temperature, a thermocouple type K class 1 from MTB Sensor-Technik was used that features a total accuracy of ± 1.5 K. In addition, a systematic error increases the uncertainty of T_0 by ± 4.0 K. The reason for this additional source of uncertainty is that the test time is shorter than the time which the thermocouple needs to reach equilibrium state at the present test conditions. As a main cause, its large response time can be stated. Hence, T_0 was extrapolated to determine the actual reservoir temperature.

The Mach-7 nozzle was employed for the present tests, the flow of which was characterized in a series of pitot pressure measurements as described in Niezgodka (2001). As a result, the cross-sectional area of the core flow slightly decreases in the direction of flow and has an average diameter of roughly 210 mm, whereby its spatial distribution of the Mach number deviates on average by ± 0.008 from the free-stream Mach number. In an additional pitot pressure measurement with a Kulite pressure transducer of the XCQ-080 series, the steadiness of the flow is analyzed at a sampling rate of 3 kHz. The standard deviation of the measured Mach number from the mean value over the free-flight period is ± 0.018 .

This study has considered the flow conditions from a previous work (Seltner et al. 2019) with single bodies. Nominal conditions of the current tests were $p_0 = 520$ kPa

and $T_0 = 600$ K resulting in a unit free-stream Reynolds number of $2.1 \times 10^6/m$. Based on these flow conditions, the free-stream conditions were determined by using the steady isentropic one-dimensional relations and the ideal gas law. Typical conditions of the experiments were a free-stream density of $\rho_\infty = 0.00787$ kg/m³, a free-stream velocity of $v_\infty = 1046$ m/s and a free-stream dynamic pressure of $q_\infty = 4307$ Pa. The total uncertainty of the free-stream dynamic pressure is ± 122 Pa by taking into account the deviation of the free-stream Mach number from the flow characterization, the total accuracy of the reservoir pressure sensor and the uncertainty due to the ideal-gas assumption of the ratio of specific heats.

2.2 Model setup

As objects of research, two blunt geometries were employed either spherical or cubical models, which were made of stainless steel with the standardized material number 1.4125 and 1.4112, respectively. It is intended that both geometries have the same mass and material density, which allows a direct comparison of the accelerations. Several test articles of both shapes were manufactured for this work. The mass was measured with a precision scale, and the moment of inertia was computed based on the actual mass and dimensions. Table 1 lists the ranges of model properties' actual values for length (as diameter and edge length), mass and transverse inertia. The average material density of the spheres is $\rho_m = 7528$ kg/m³. For the application of the present marker-based stereo-tracking technique, a random arrangement of matt-black circular point markers on a matt-white surface is varnished on the models.

Figure 2 depicts the frame of reference, where x , y and z are the Cartesian coordinates as well as g is the gravitational acceleration. The definition of the reference frame is needed to determine their aerodynamic coefficients of lift force C_L , drag force C_D and pitching moment C_M , whereby the subscripts 1 and 2 represent the primary (leading) and secondary (trailing) object. The origin of the right-handed global coordinate system (GCS) here is spatially fixed in the center of the nozzle's exit plane. It has the positive x -axis pointing downstream, the y -axis in the transverse direction and the positive z -axis pointing vertically up. Body-fixed local coordinate systems (LCS) are defined in the centers of gravity (CoG)

Table 1 Actual value ranges of model properties

Property	Sphere	Cube
Length (mm)	50.37 ± 0.05	40.91 ± 0.07
Mass (g)	503.75 ± 0.15	505.29 ± 1.02
Transverse inertia (10^{-4} kg m ²)	1.278 ± 0.002	1.409 ± 0.008

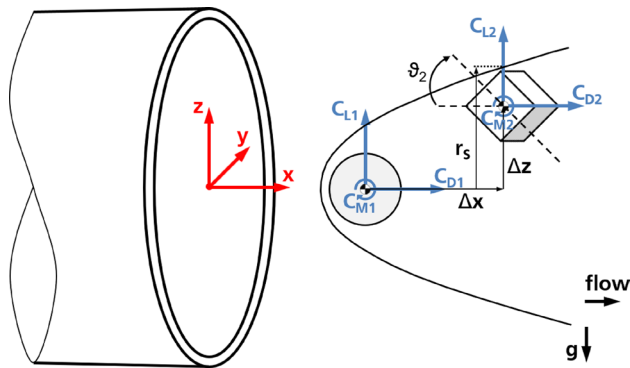


Fig. 2 Nomenclature and definition of global coordinate system with respect to nozzle exit for the example of a sphere-cube configuration

of both free-flying objects so that the x -axis of the sphere is parallel to the global x -axis at $t = 0$ s, while the x -axis of the cube is normal to one of its sides. It is expected that the model motions for the present experimental setup occur in an xz -plane. Hence, the main influence factor in this study is the relative distance between primary and secondary body in x - and z -direction (shown in Fig. 2), namely streamwise (Δx) and vertical (Δz) separation distance. Another investigated parameter for cubical bodies is the pitch angle θ , which designates the inclination between the global x -axis and one cube's surface normal. Here, $\theta = 0^\circ$ means that one surface is orthogonal to the flow. The positive direction of rotation is clockwise by viewing along the y -axis.

In addition, the shock radius r_s is shown in Fig. 2. This parameter represents the radius of the primary bow shock at the position of the secondary object being calculated with the modified equation for the shock shape by Billig (1967) proposed by Prévereaud (2014).

2.3 Free-flight technique

A well-established free-flight technique was employed for the present experiments enabling a synchronous release of two models with subsequent entirely free movement of them in the flow. By the use of this technique, aerodynamic interferences due to a sting support or a balance are prevented. An experimental setup in the H2K's test section using the free-flight technique is provided in Fig. 3, where the initial positions of two sphere-cube pairs on the model dropping system are shown in the upper right corner. In general, the initial positioning below refers to the setting at the start of the experiment. In the beginning, the measurement chamber is under vacuum condition, while each test article is held by an electromagnet located at the chamber ceiling. The initial pitch angle θ_0 here is defined by the model alignment on the holder. In order to facilitate a precise model alignment and angle adjustment, a fixed mounting support for different

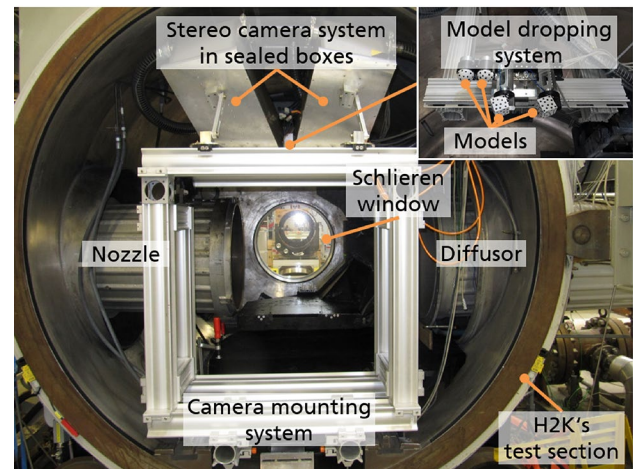


Fig. 3 Experimental setup in H2K's test section

single orientations is employed to cover a large variety of pitch angles. After initiating the flow, the free jet needs 2 to 3 s to reach the desired flow conditions. When this state is achieved, the test articles are released from the holders and fall in vacuum. When passing the top shear layer, the increasing stagnation pressure causes an inhomogeneous pressure distribution on the model surface leading to a positive lift force as well as a rotation of the body, especially the cube. Subsequently, the effective test time begins as soon as the trailing object is completely within the homogeneous core flow and ends as soon as it reaches the edge of the core flow. At the end, both models cross the lower part of the shear layer before they are caught at the bottom of the test section. For the current experimental setup, one to two releases of model pairs were carried out per run of the facility with the aim to decrease the operational costs. A time delay between the drops is satisfied that guarantees a steady-state free jet for each free flight.

2.4 Instrumentation

High-speed schlieren videography was used to characterize the flow field. A single-path Z-type schlieren setup with a high-speed camera was used as described in Daub (2023) that is suited to capture sharp images. As a light source, a 1000 W xenon arc lamp was employed. A Photron FASTCAM APX-RS model 250K high-speed camera with a monochrome CMOS sensor was used. The camera was set to the maximum frame rate of 3 kHz at full image resolution of 1024×1024 pixels and an exposure time of $4 \mu\text{s}$ for the present tests.

A high-speed stereo-tracking system based on the detection of marker points on the model surface was applied to reconstruct the three-dimensional flight trajectory and

attitude of the freely flying test articles. Two synchronously capturing cameras in stereoscopic arrangement were placed inside the test section above one schlieren window. They have a view on the measurement volume at an angle of roughly 60° against the horizontal plane in order to avoid obstructing the schlieren path. Both cameras were the Photron FAST-CAM SA-X2 model 1080K, which were operated with a full frame resolution of 1024×1024 pixels at a frame rate of 12 kHz. Each camera was equipped with 24-mm-focal-length lenses ensuring the observation of a measurement volume of $540 \times 580 \times 580$ mm for the present measurement distance of roughly 650 mm. These two cameras were enveloped in sealed boxes and supplied with external cooling air to prevent overheating due to the surrounding vacuum during the operation of facility. To provide sufficient illumination, each camera was outfitted with four 86 W and four 38 W high-power LEDs on a capacitive cooling ring, which was concentrically mounted on the optical window of the protective box.

2.5 Data processing

For the purpose of determining the models' center-of-gravity positions and body orientations in 3D space, the captured sequence of synchronous image pairs from the stereo-tracking cameras is employed. The point-based DIC technique is used by the commercial stereo-tracking software ARAMIS Professional 2017 providing three-dimensional and time-resolved data that offers precise coordinates and displacements for either a single point or a group of points within a measurement volume by the principle of triangulation. This software facilitates a 6DoF analysis of deformations and motions in general. ARAMIS is applied in the present activities to determine the three positions in streamwise (x), spanwise (y) and vertical (z) direction as well as the orientations roll (φ), pitch (ϑ) and yaw (ψ) angle of both models with respect to the GCS. With the current approach, a calibration deviation of $2 \mu\text{m}$ is achieved. The true accuracy of the stereo-tracking system is determined in an additional reference measurement with the same experimental setup and flow conditions as in the wind tunnel tests (Seltner et al. 2019), whereby the resulting standard deviations in x -, y - and z -direction are $16 \mu\text{m}$, $31 \mu\text{m}$ and $48 \mu\text{m}$, respectively.

The translational and angular velocities and accelerations of the test objects are computed based on the time-resolved motion data by filtering and differentiating. Discrete differentiations are performed by central finite difference quotient. A conventional Savitzky–Golay filter with a first-order polynomial and subsets of 201 data points (equivalent to 17 ms) was used to smooth the data before differentiation, that promises the best results after a careful analysis of parameters. This particular filter type was chosen to remove higher frequency components.

Unlike the procedure described in the previous paragraph and in previous studies (Seltner et al. 2019, 2021), the motion data of WSI configurations exhibit a singularity in the measured signals due to a short impulse when the objects collide. This would result in strong distortions of the motion derivatives in the neighborhood of the singular point. For this reason, the moment in time of the collision is determined, and the datasets before and after it are post-processed separately for each component of motion. The singular point is calculated by finding the discontinuity in the second derivative of streamwise position data. Since the points at the start and the end of the series can be just insufficiently calculated with the conventional Savitzky–Golay filter due to artificial extensions, the noise reduction is weaker for data points close to the moment of collision. Hence, the last points before the impact as well as the first points after it are filtered by polynomial fittings with specified constraints in contrast to the other part of the dataset being smooth by the Savitzky–Golay filter. In the course of this, a third-order polynomial is applied to fit it to the edges of measurement data, which fulfills a set of constraints concerning the same value in position, velocity and acceleration at the intersection of Savitzky–Golay-filtered and polynomial-fitted motion data as well as the same accelerations of the two datasets at the point shortly before and after the collision event. Following this, both parts of the data are merged before differentiation using the common procedure with central finite difference quotients. After each differentiation, the polynomial order of fitting is reduced by one. The Savitzky–Golay filter has the same settings as for the SSI configurations, except that a polynomial order of 2 is assumed for the first filtering of the position signals.

In order to calculate the aerodynamic coefficients, the test time was chosen so that the flow conditions are steady-state and the trailing model is completely within the core flow (as described in Sect. 2.3), minimizing uncertainties due to changes in the flow conditions. The force and moment coefficients are calculated with the equations as in Seltner et al. (2019), where the reference area S_{ref} in this study is defined as the circle projected area ($S_{ref} = \pi r^2$) for spheres and the square base area ($S_{ref} = l^2$) for cubes. To calculate the moment coefficient, the sphere's diameter or the cube's edge length is used as the reference length l_{ref} . The vertical (z) force component is separated from gravity in order to determine the lift coefficient.

3 Results & discussion

Various arrangements of tandem body pairs are investigated in the following analysis. The purpose is to develop an understanding of the dynamical motion behavior and the flow topology during aerodynamic interaction with

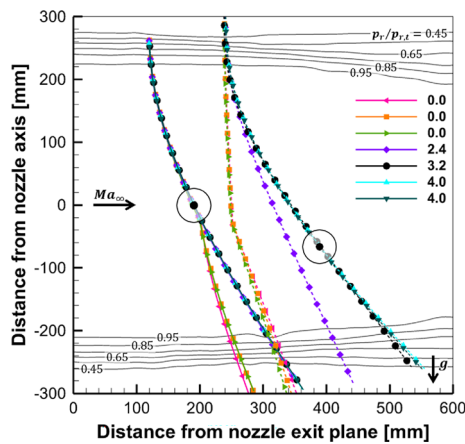


Fig. 4 Flight trajectories of leading (solid lines) and trailing spheres (dashed lines) with different initial vertical positions at $\Delta\hat{x}_0 = 4.8$ including flow field characteristics of H2K's Mach-7 nozzle

focus on the impact of body shape and inclination. Two different types of configurations are distinguished with in-line arrangements for the analysis of WSI and out-of-line formations for the study of SSI. This distinction is made due to the fact that different flow phenomena and separation characteristics are expected to emerge in each case. Shock-shock interactions are presented in Sect. 3.1 and wake-shock interactions in Sect. 3.2. Figure 4 depicts the flight trajectories of sphere pairs in the xz -plane with an initial streamwise distance of 0.12 m overlaying the experimental ram pressure distribution of the free jet as contour lines. Here, p_r is the local ram pressure from a series of pitot pressure measurements and $p_{r,t}$ represents the theoretical quantity that is defined as the adiabatic stagnation pressure behind a normal shock based on the reservoir pressure. Please note that the core flow is defined by the area between the contour lines with $p_r/p_{r,t} = 0.95$. At the first glance, all trajectories show an intersection for the leading and trailing body in the beginning as well as a divergence in the middle and lower region of the core flow. There are clear differences between the two configurations, whereby the trailing objects of the in-line formations experience a barely noticeable motion in flow direction as well as a collision with the leading body (see, e.g., orange lines), whereas they mostly undergo a significant higher streamwise displacement than the leading sphere for the out-of-line cases (see, e.g., black lines).

In the subsequent analysis, non-dimensional quantities for position and velocity data are depicted. Data are presented in the form of normalized separation distances, defined as:

$$\Delta\hat{x} = (x_2 - x_1)/r, \tag{2}$$

$$\Delta\hat{z} = (z_2 - z_1)/r, \tag{3}$$

where the radius of the sphere r is 0.025 m. A value of $\Delta\hat{x} = 2.0$ corresponds to the body contact of two axially aligned spheres.

The normalized time \hat{t} and separation velocities in streamwise (\hat{v}_x) as well as in vertical (\hat{v}_z) direction are defined as follows:

$$\hat{t} = \sqrt{\rho_\infty / \rho_m} t v_\infty / r, \tag{4}$$

$$\Delta\hat{v}_x = \sqrt{\rho_m / \rho_\infty} (v_{x2} - v_{x1}) / v_\infty, \tag{5}$$

$$\Delta\hat{v}_z = \sqrt{\rho_m / \rho_\infty} (v_{z2} - v_{z1}) / v_\infty. \tag{6}$$

For the final lateral velocity \hat{v}_T , reversed signs of the primary and secondary body's velocities are used in order to indicate repulsive separation behavior by positive signs, defined as:

$$\hat{v}_T = \sqrt{\rho_m / \rho_\infty} (v_{z1} - v_{z2}) / v_\infty. \tag{7}$$

3.1 Shock-shock interaction

Experimental results of out-of-line formations with spheres and cubes are presented in the following (see test matrix in Table 2), which give an insight into the influence of body shape and inclination on stable shock-wave surfing in the presence of SSI. In the following, the flow topology (see Sect. 3.1.1) in combination with the corresponding measurement results of motion data (see Sect. 3.1.2) and aerodynamic coefficients (see Sect. 3.1.3) are presented for an exemplary test case. Afterward, the separation behavior between a leading and trailing body (see Sect. 3.1.4) is

Table 2 Test matrix of SSI configurations

Primary shape	Secondary shape	ϑ_{01} (°)	ϑ_{02} (°)	$\Delta\hat{x}_0$ (-)	$\Delta\hat{z}_0$ (-)
Sphere	Sphere	N/A	N/A	4.8	0.0
Sphere	Sphere	N/A	N/A	4.8	2.4
Sphere	Sphere	N/A	N/A	4.8	3.2
Sphere	Sphere	N/A	N/A	4.8	4.0
Sphere	Sphere	N/A	N/A	4.8	5.0
Sphere	Sphere	N/A	N/A	7.2	3.2
Sphere	Sphere	N/A	N/A	7.2	4.0
Sphere	Cube	N/A	-30	4.8	4.0
Sphere	Cube	N/A	-30	7.2	4.0
Sphere	Cube	N/A	-20	4.8	4.0
Sphere	Cube	N/A	-20	7.2	4.0
Sphere	Cube	N/A	+0	4.8	4.0
Sphere	Cube	N/A	+0	7.2	4.0
Sphere	Cube	N/A	+45	4.8	4.0
Sphere	Cube	N/A	+45	7.2	4.0
Cube	Cube	+20	+0	4.8	4.0

examined. The next part look at the effect of body shape and inclination (see Sect. 3.1.5). Finally, the system dynamics of SSI (see Sect. 3.1.6) are discussed.

3.1.1 Flow topology

Figure 5 provides sequences of schlieren image with sphere–sphere (Fig. 5a), sphere–cube (Fig. 5b) and cube–cube (Fig. 5c) configurations with almost the same initial positioning. For each image sequence, the time between the first and last recording is 4/75 s. A pitch rotation of the cubes in the counter-clockwise direction due to the impact of the free jet’s top shear layer can be seen in the images. From the schlieren images, it is apparent that cubes experience more streamwise displacement than spheres, regardless of whether these are leading or trailing objects, as expected. As a result, the trailing cubes are outside the viewing area of the schlieren image in the third snapshot of the sequence (see Fig. 5b and c) unlike the spheres (see Fig. 5a). In the flow fields of both bodies, detached bow shocks are visible, which undergo different Edney’s types of shock-shock interaction depending of the relative position. For example, Fig. 5a shows the Edney type IV interaction, Fig. 5b depicts the types III and IV, and Fig. 5c shows the types V and VI. Interestingly, two more shock-shock interactions can be seen just for the cube–cube configuration in Fig. 5c. Multiple simultaneous shock-shock interactions in a two-body configuration have been apparently observed for the first time. The reattachment shock as well as the shock from the compression waves of the primary body interacts with the secondary bow shock in each case, that result in visible

deformations of the bow shock. Additionally, it can be seen that the bow shock of the trailing object becomes weaker until it disappears in the region of the primary wake region (see, e.g., second image of Fig. 5c).

For a typical SSI configuration with two spheres, a sketch of the supersonic flow phenomena with the corresponding schlieren image in the background is presented in Fig. 6, where the normalized separation distance is 4.8 in x -direction and 4.0 in z -direction. In doing so, the entire flow field of the leading object is identical to that of a single sphere as

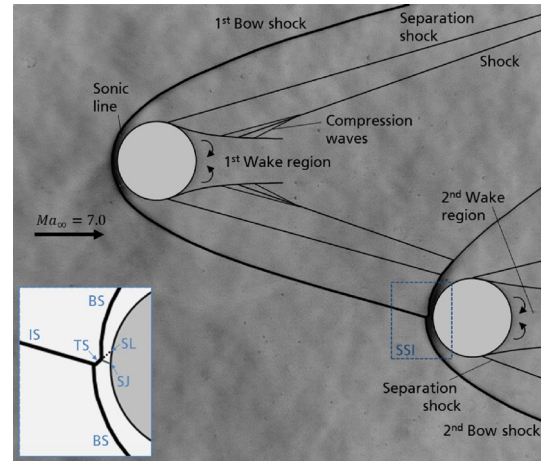
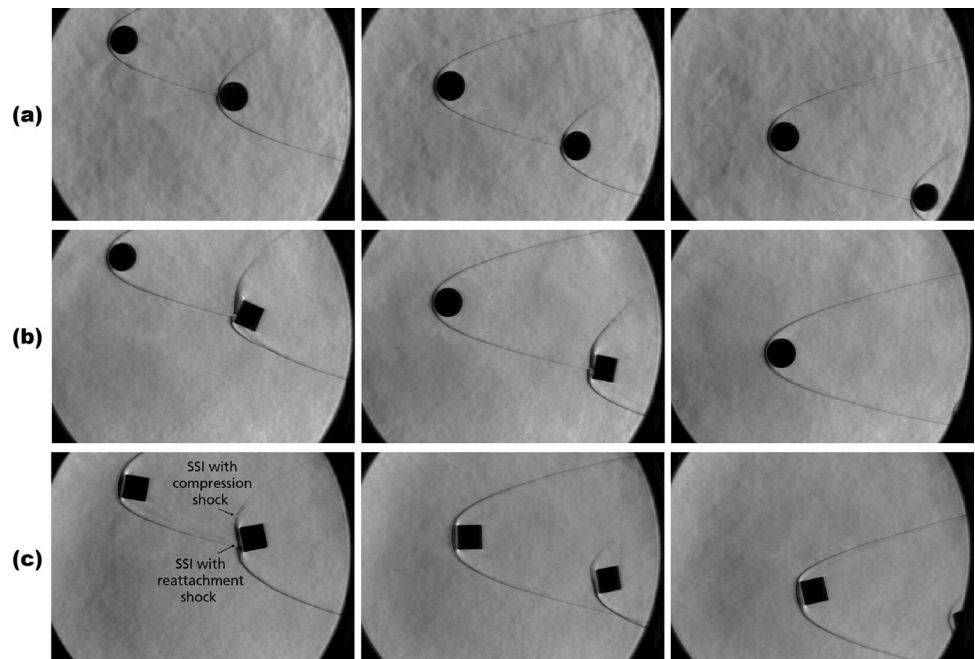


Fig. 6 Qualitative flow field of a secondary sphere located on the shock wave behind a primary sphere with $\Delta\hat{x} = 8.2$ and $\Delta\hat{z} = 4.0$ including schematic description of flow structures with bow shock (BS), impingement shock (IS), transmitted shock (TS), supersonic jet (SJ) and shear layer (SL)

Fig. 5 Selection of schlieren image sequences showing the motion behavior in free-flight for different tandem body pairs at $\Delta\hat{x}_0 = 4.8$ and $\Delta\hat{z}_0 = 4.0$: **a** sphere–sphere (S–S), **b** sphere–cube (S–C) with $\vartheta_{02} = -30^\circ$ and **c** cube–cube (C–C) with $\vartheta_{01} = 20^\circ$ and $\vartheta_{02} = 0^\circ$



in (Van Dyke 1982), which indicates that the trailing body has no influence on the upstream flow field of the leading body. By contrast, the flow around the trailing sphere changes due to aerodynamic interactions as shown before. The shock–shock interaction of both bow shocks in the present case can be classified as type IV according to Edney (1968). It is also apparent from Fig. 6 that the wake region of the trailing spheres becomes asymmetric due to the inhomogeneous inflow as well as the visible intensity of the second bow shock decreases inside the region enclosed by the shock as a result of the lower Mach numbers in the wake.

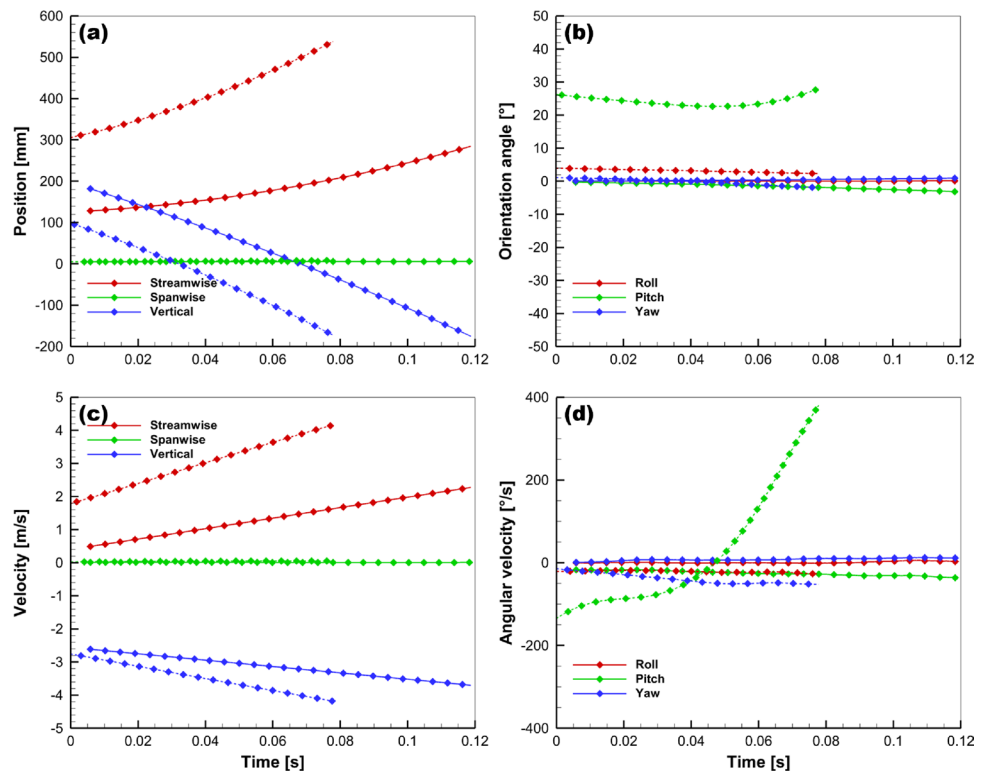
3.1.2 Model motions

A single example for the displacement and velocity data of a front sphere and an aft cube with an initial offset in z -direction is depicted in Fig. 7 that consist of the three-dimensional motion data with respect to their translation and their rotation. It is apparent that the trailing object enters the H2K’s core flow some milliseconds before the leading one in all of the investigated tests. As a consequence, the shock–shock interaction on the trailing body is not fully established until the leading body has passed the shear layer and is fully in the core flow. To assess the alignment accuracy, the relative distances between both bodies in y -direction are examined, which exhibit a maximum deviation of 2.8 mm. Thus, it can be assumed that both objects are approximately in the same xz -plane during free flight,

since the effect of the misalignment on the measurement uncertainty in the drag coefficient is less than 0.3% referred to the single-body value. In doing so, both roll, yaw and spanwise motion components are almost zero over the entire free-flight time unlike both streamwise and vertical motion components. For example, the changes of the trailing body in streamwise position ($\Delta x_2 = 280.6$ mm) and vertical position ($\Delta z_2 = -368.0$ mm) are about two orders of magnitude higher than the changes in spanwise position ($\Delta y_2 = 3.5$ mm) as shown in Fig. 7a and b, while the absolute changes in roll angle ($\Delta \varphi_2 = -2.3^\circ$) and yaw angle ($\Delta \psi_2 = -2.7^\circ$) are less than 3° . Thus, the analysis can be reduced to a two-dimensional motion. Consequently, the subsequent analysis in this work treats the motion as 3DoF (streamwise, vertical and pitch displacement) and neglects the out-of-plane motion (roll, yaw and spanwise displacement). In addition, the orientation angles for configurations with only spheres are neglected, as the maximum absolute changes in roll, pitch and yaw angle are less than or equal to 2° .

As shown in Fig. 7c and d, the absolute values of translational and angular velocities increase over time except for the spanwise component. Contrary to the assumption, the angular velocities of out-of-plane motion components shown small deviations from zero, which indicates the high sensitivity of SSI on the motion derivatives due to very small deviations in alignment.

Fig. 7 Evolution of 6DoF translational and angular motion data in core flow of a leading sphere (solid lines) and a trailing cube (dashed lines) at $\vartheta_{02} = 45^\circ$ with $\Delta \hat{x}_0 = 4.8$ and $\Delta \hat{z}_0 = 4.0$: **a** positions, **b** orientation angles, **c** velocities and **d** angular velocities



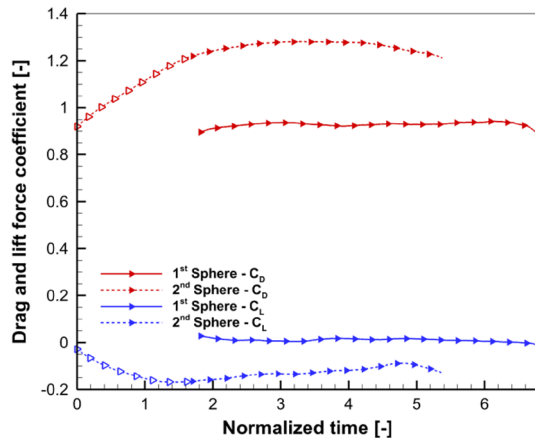


Fig. 8 Exemplary evolution of drag (red) and lift force coefficients (blue) in core flow of a primary (solid lines) and a secondary sphere (dashed lines) with $\Delta\hat{x}_0 = 4.8$ and $\Delta\hat{z}_0 = 4.0$; open symbols indicate a leading body in top shear layer

3.1.3 Aerodynamic forces

Drag and lift force coefficients of a leading and trailing sphere in an out-of-line formation are plotted against the normalized time in Fig. 8. The pitching moment coefficients of both models are approximately zero and are therefore not depicted. Small deviations from the constant drag coefficient can be seen at the edges of leading body's graph, which are a minor effect of the free jet's shear layer. As expected, the drag coefficient of the leading sphere matches on average with the single-body value of $C_D = 0.926$ (Seltner et al. 2018), while the lift coefficient is nearly zero. It is notable that the drag coefficient of the secondary body increases steadily from $C_{D2} = 0.92$ to 1.22 in the beginning because of the aforementioned weaker aerodynamic interaction, as long as the leading object is located in the free jet's shear layer in contrast to the trailing object. Subsequently, the trailing drag coefficient yet reaches a roughly constant value as soon as both objects are inside the core flow of the free jet having a maximum value of $C_{D2} = 1.28$. These results are in line with those of previous studies (e.g., Laurence et al. 2012). Regarding the trailing lift force, it can be seen in Fig. 8 that a reduction of its coefficient over time emerges first due to the appearing interaction, followed by a rise due to the entrainment tending to zero.

3.1.4 Separation behavior

Prior studies have noted the importance of the relative positioning on the separation behavior of multiple bodies. Figure 9 shows the flight trajectories of the trailing spheres plotted as $\Delta\hat{z}$ (see Eq. 3) against $\Delta\hat{x}$ (see Eq. 2) for different initial spacings. Please note that the two spheres relatively move away from each other in x -direction and slightly

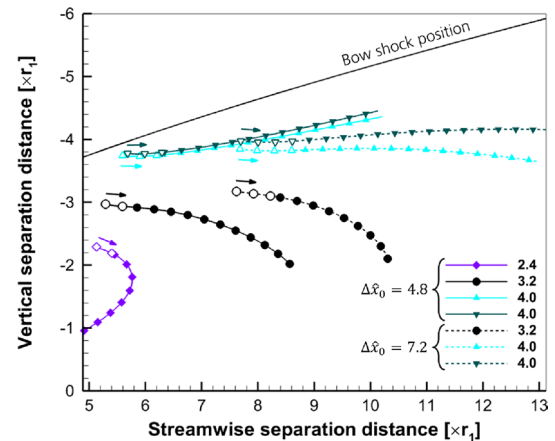
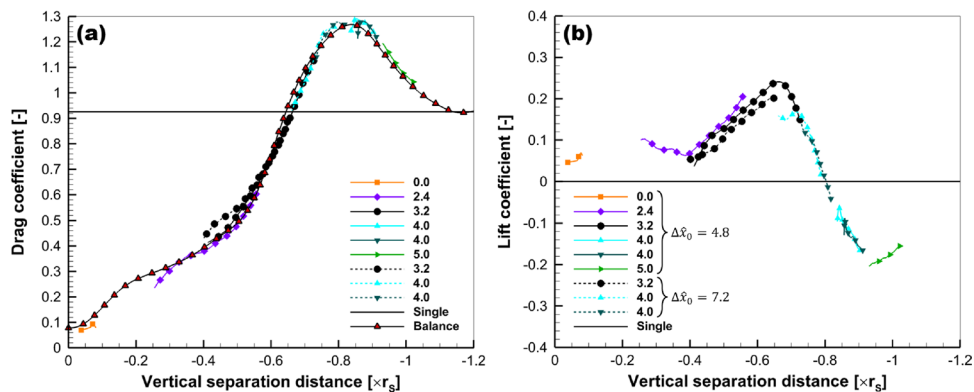


Fig. 9 Normalized flight trajectories of trailing spheres related to leading spheres in core flow (closed symbols) and bottom shear layer (open symbols) for different initial vertical positions at $\Delta\hat{x}_0 = 4.8$ (solid lines) and $\Delta\hat{x}_0 = 7.2$ (dashed lines)

toward each other in z -direction before entering the core flow because of the shear-layer-influenced aerodynamic loads. What stands out in the chart of relative trajectories is that the streamwise separation distance rises in all out-of-line cases. This is due to an increase of the surface pressure on the secondary body as a result of the flow structures behind two interacting bow shocks. The variation of the initial vertical component reveals that the greater the lateral distance of the secondary sphere to the primary sphere in combination with a higher axial distance, the greater the increase in the streamwise separation distance over approximately the same period of time. In consequence, the trailing bodies tend to move into different flow regions of the leading objects after aerodynamic interaction. For $\Delta\hat{z}_0 = 2.4$ and $\Delta\hat{z}_0 = 3.2$, the trailing sphere moves away from the leading sphere in streamwise direction and then tends to move toward it. In doing so, the trailing sphere reaches the near-wake more quickly in the test cases with $\Delta\hat{z}_0 = 2.4$ (see purple line) than with $\Delta\hat{z}_0 = 3.2$ (see black line). Increasing the initial vertical separation distance to $\Delta\hat{z}_0 = 4.0$ results in shock-wave surfing, whereby the secondary sphere ends in the far-wake for $\Delta\hat{x}_0 = 7.2$ (see cyan and blue-gray dashed lines) afterward or continues to interact with the shock for $\Delta\hat{x}_0 = 4.8$ (see cyan and blue-gray solid lines). The necessary condition according to Marwege et al. (2018) for shock-wave surfing is fulfilled for the tests with $\Delta\hat{x}_0 = 4.8$ and $\Delta\hat{z}_0 = 4.0$, but this only applies to the last third of the data. Previous studies such as Register et al. (2020) have identified the near-wake, the far-wake and the shock region as final zones, which is consistent with the present results.

Figure 10 shows the drag and lift coefficients of the trailing sphere for multiple tests with different initial streamwise and vertical distances. In doing so, the data are plotted against the normalized vertical separation distance based on

Fig. 10 Influence of vertical separation distance on trailing sphere’s force coefficients based on force-balance and stereo-tracking measurements at $\Delta\hat{x}_0 = 4.8$ (solid lines) and $\Delta\hat{x}_0 = 7.2$ (dashed lines): **a** drag and **b** lift; vertical separation distance is normalized with shock radius



the calculated shock radius. The results show a strong impact of the vertical separation distance on both force coefficients, whereas the moment coefficients are not shown as they were found to be negligibly small with $|C_{M2}| < 0.005$. The drag coefficient continuously increases from $C_{D2} = 0.07$ for axially aligned bodies to 1.29 during the shock-wave surfing, which is 39.3% more than the single-body value without aerodynamic interactions. As regards the lift coefficient, this quantity is positive (attractive force) with a peak of $C_{L2} = 0.24$ until the zero-crossing at $\Delta\hat{z} = -0.80$ and turns to negative coefficients (repulsive force) afterward. The comparison of the absolute difference between single-body and peak value of the drag and lift coefficients shows that neither a general dominance of the streamwise nor the lateral separation is apparent for two identical spheres. The most striking result to emerge from the coefficient data is that the curves at the same vertical separation distances (compare black solid and dashed line with circles in Fig. 10) are in very good agreement, although the streamwise separation distance differs on average by approximately two times the radius (see black lines in Fig. 9). It follows that the drag and lift coefficients are less sensitive to the streamwise separation distance than to the vertical component. This is reasonable, because the shock angle β of the primary bow shock changes less further downstream for tandem configurations

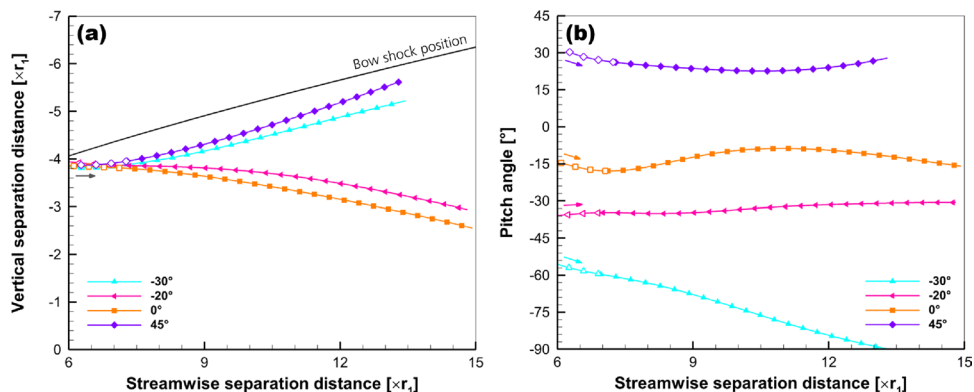
in contrast to proximal bodies. For SSI cases that have the same distance of the secondary body to the primary bow shock, the shock angle mainly influences the aerodynamic force coefficients. As a result, it can be assumed that the sensitivity decreases with increasing streamwise separation distance, since the shock angle converges.

To validate the aerodynamic coefficients determined with the stereo-tracking method, experimental force-balance measurements of Willems et al. (2018) with a free-flying leading sphere and a fixed trailing one are also presented in Fig. 10a. In comparison, the drag coefficients of both measurement methods are in very good agreement, although their streamwise distances from each other differ by up to 7 times the sphere radius as well as the wake of the secondary sphere is disturbed by the balance. Nevertheless, it is known that the sting effects are negligible in hypersonic wind tunnel, whereby the drag for this setup with a balance is 0.1% less than without mounting supports (Taguema 2017).

3.1.5 Effect of body shape & inclination

To understand the effect of body shape and inclination on the separation behavior, the trailing sphere is replaced by a cube with nearly equal mass and a variation of its initial

Fig. 11 Normalized flight trajectories **a** and pitch angles **b** of trailing cubes related to leading spheres in top shear layer (open symbols) and core flow (closed symbols) for different initial pitch angles at $\Delta\hat{x}_0 = 4.8$ and $\Delta\hat{z}_0 = 4.0$



pitch angle is carried out. In Fig. 11, relative flight trajectories in the xz -plane and their corresponding pitch angles are illustrated for different initial inclinations of sphere–cube pairings with $\Delta\hat{x}_0 = 4.8$. What stands out in Fig. 11 is that the separation distance and pitch angle highly depend on the shape and initial orientation for the same nominal initial positions. Concerning the translational component in Fig. 11a, the trailing cube experiences an immediate entrainment within the primary bow shock for $\vartheta_{02} = -20^\circ$ and $\vartheta_{02} = 0^\circ$, a slow expulsion from the primary bow shock for $\vartheta_{02} = 45^\circ$ as well as an extended shock-wave surfing for $\vartheta_{02} = -30^\circ$. For the latter, the necessary condition for stable shock-wave surfing ($\tan\beta = \frac{\Delta a_z}{\Delta a_x}$) is satisfied. After aerodynamic interactions, these objects tend to end in the far-wake, the aerodynamically independent region and the shock region, respectively. The results also show a correlation between the final vertical separation distance and the absolute initial pitch angle starting from the orientation of plane-exposed to edge-exposed, which is also consistent with the results of tests at $\Delta\hat{x}_0 = 7.2$. This relationship may be explained by the fact that the induced lift force due to the body inclination is positive (attractive) for pitch angles larger than -45° and negative (repulsive) for pitch angles smaller than -45° (see Fig. 14 in Seltner et al. (2019)). In the case of shock-wave surfing, a trailing cube roughly traces the same trajectory referred to the leading sphere just like a trailing sphere (compare cyan solid line in Fig. 11a with cyan solid line in Fig. 9). Thereby, the cube undergoes an increased streamwise separation in nearly the same time. Concerning the angular component in Fig. 11b, the secondary body’s pitch angle experiences an oscillation for $\vartheta_{02} = 0^\circ$, a slight uniform increase for $\vartheta_{02} = -20^\circ$, a rapid decrease for $\vartheta_{02} = -30^\circ$ as well as a reversal of the rotational direction for $\vartheta_{02} = 45^\circ$. As a result, the pitch motion is affected by the pitching moment induced by the orientation of the body as well as by the SSI between both objects as previously shown for the lateral separation. This finding is reasonable, since Edney type III and IV interactions can produce very high local pressures on the surface (Edney 1968) and it is well known that the aerodynamic moments are very sensitive to the exact pressure distribution. Consequently, the position of the impingement point strongly influences the magnitude and sign of the superposed pitching moment and also the lift force. Hence, the aerodynamic load through the body inclination can cause an amplification or attenuation of the pitch and vertical displacement, which explains the different types of motion.

The results for the normalized vertical separation velocity are shown in Fig. 12. It should be noted that negative values represent repulsive motion tendencies regarding the vertical component, since the measured vertical separation distances are negative as the aft object enters the flow first. First of all,

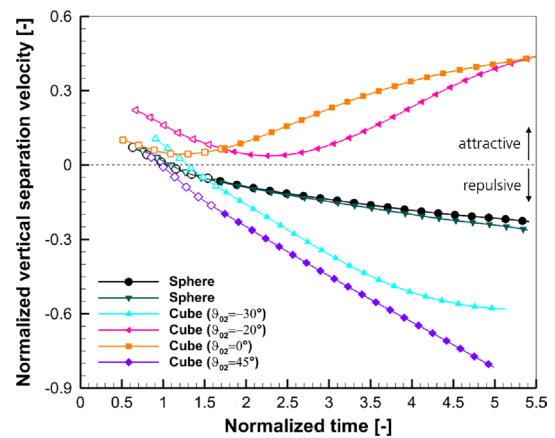


Fig. 12 Evolution of trailing body’s normalized vertical separation velocity with view to a leading sphere in top shear layer (open symbols) and core flow (closed symbols) for different configurations at $\Delta\hat{x}_0 = 4.8$ and $\Delta\hat{z}_0 = 4.0$

Table 3 Experimental normalized final lateral velocities \hat{v}_T and Passey’s constants C for various shapes and initial pitch angles ϑ_{02}

Shape	ϑ_{02} (°)	\hat{v}_T (-)	C (-)
Sphere	N/A	+0.246	0.040
Cube	-30	+0.581	0.183
Cube	-20	-0.037	N/A
Cube	+0	-0.042	N/A
Cube	+45	+0.815	0.360

it can be seen that the velocity curves tend to values close to 0.3 at $\hat{t} = 0$, which is the result of the positive lift force due to the shear layer as aforementioned. Just as already shown for the separation distance and the pitch angle, a major difference between various initial inclinations was found for the vertical separation velocity in terms of the observed motion behavior. On the one hand, the curves of the trailing cubes with $\vartheta_{02} = -30^\circ$ and $\vartheta_{02} = 45^\circ$ increase more steeply and reach higher peak values than those of sphere–sphere arrangements that feature shock-wave surfing. The peaks in Fig. 12 are higher compared to those of other studies with side-by-side test cases like by Li et al. (2015) or Park et al. (2021). On the other hand, the vertical separation velocity for sphere–cube configurations with $\vartheta_{02} = -20^\circ$ and $\vartheta_{02} = 0^\circ$ turns into increasing attractive values as soon as the trailing cube is fully entrained within the region bounded by the primary bow shock. The strong impact of the initial pitch angle is related to the induced lift force due to the body inclination.

The final lateral velocity here is defined as the peak value of the repulsive vertical separation velocity attained in the H2K’s core flow. Table 3 reports the normalized final lateral velocity \hat{v}_T and the Passey’s constant C based on Eq. (1) for different configurations of the trailing body. Comparing the present results with those from Laurence et al. (2012), the

value of \hat{v}_T is identical in the case of two equal spheres and the constant is in the range identified by Passey and Melosh (1980). For trailing cubes, it is remarkable to see that the non-dimensional parameters in Table 3 are higher than for spherical bodies and depend on the initial pitch angle, while the normalized final lateral velocity of cubes is two to three times larger than that of spheres. However, this result differs from Park et al. (2021), who found significantly lower values for side-by-side configurations representative of the position after an actual fragmentation event.

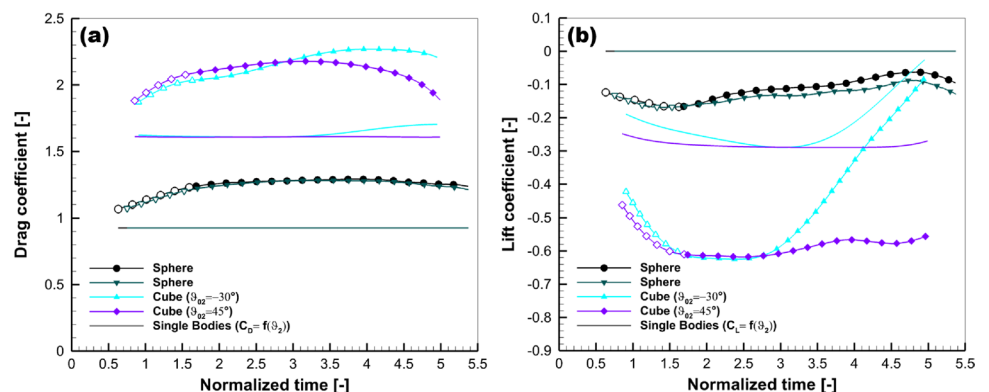
Closer inspections of the force coefficients should aid to find the cause of cube’s higher separation velocities. For this reason, the drag and lift coefficients over the normalized time of tests with occurring shock-wave surfing are compared in Fig. 13 with single-body values calculated with the correlations of (Seltner et al. 2018, Eqs. (5) and (6)) using the secondary body’s pitch angle measured in this work. It is apparent from this figure that the extreme values of the force coefficients are in general higher in terms of shock–shock interaction. Interestingly, the relative increases of the drag coefficient in Fig. 13a with respect to the single-body value tend to 40% regardless of the trailing object’s shape. However, the maximum value of the cubes is nearly twice as much as that of the spheres resulting in a faster streamwise separation. Regarding the lift coefficient in Fig. 13b, it is noticeable that this quantity approximately doubles for cubes in comparison with the single-body value at the same pitch angle. By comparing the lift coefficients of both body shapes, the peak value of the trailing cubes is even three times as large as that of the spheres. It can therefore be concluded that the lateral separation is determined by the shock–shock interaction as well as the induced lift force due to the body inclination of non-spherical bodies. This study confirms the initial finding of two superimposed effects by Park et al. (2021). As a result, the discrepancy between real-world observations and previous laboratory studies with only spherical bodies can be explained by the current finding to some extent.

In conclusion, the body orientation of a rotating non-spherical secondary object in the present study causes an increase in the final lateral velocity and streamwise displacement in the case of shock-wave surfing, which is consistent with Li et al. (2015). This is expected, since the lift force due to the inclination is zero for cubes in statically stable trim flight attitudes, whereas a rotating body can effect a strong attractive lift force depending on its orientation.

3.1.6 System dynamics

In order to analyze the stability behavior of tandem bodies in SSI configurations, an appropriate frame of reference based on the position of primary bow shock was applied as per Eq. (8) and (9), which are similar to that of Laurence and Deiterding (2011). Here, \hat{r}_S represents the shock radius, which is normalized by the sphere radius and varies as a function of $\Delta\hat{x}$. This is also true for the shock angle, as the bow shock has a curvature. Thus, the normalized vertical shock distance $\hat{\eta}$ is the distance in z -direction between the center of the secondary model and the position of primary bow shock as a multiple of the sphere radius. The shock angle is time-dependent, because the trailing body changes its relative streamwise distance to the leading body over time. However, the maximal differences in the shock angle from start to end of free-flight are less than 3° in the present tests, which results in a maximum change in the vertical shock velocity \hat{v}_η of 6.8% relative to the maximum change in the vertical shock velocity that neglects the dependence of shock angle and streamwise separation distance. As a consequence, the influence of the aerodynamic forces on shock-wave surfing is significantly higher here than of the shock curvature, which is why the effect of the shock angle on the stability enhancement is neglected in the following. Hence, the system of differential equations related to the relative translational motion between two spheres can be simplified to a two-dimensional approach to enable a phase-plane analysis. Please note here that the phase space of the sphere–cube cases has a higher dimension due to the

Fig. 13 Comparison of trailing object’s force coefficients in terms of leading spheres in top shear layer (open symbols) and core flow (closed symbols) with $\Delta\hat{x}_0 = 4.8$ and $\Delta\hat{z}_0 = 4.0$ and single-body values (no symbols) from Seltner et al. (2018) based on measured pitch angle: **a** drag and **b** lift



influence of the pitch angle on the aerodynamic coefficients, which is why a two-dimensional projection is used for the graphical representation to enable a direct comparison with the sphere–sphere pairs.

$$\hat{\eta} = \Delta\hat{z} - \hat{r}_S \tag{8}$$

$$\hat{v}_\eta = \Delta\hat{v}_z - \tan\beta\Delta\hat{v}_x, \tag{9}$$

Figure 14 presents multiple phase paths of the trailing object’s motion for spheres and cubes in different initial configurations. Stationary points lie at $\hat{v}_\eta = 0$ enabling shock-wave surfing, whereas positive values indicate an instantaneous tendency toward expulsion of the trailing body from the region bounded by the primary bow shock while negative values suggest a tendency toward entrainment. With regard to the stability of shock-wave surfing, the phase path moves around the stationary point for a stable state, whereas the phase path approaches the stationary point along one direction and moves away from it along the other direction for an unstable state.

For trailing spheres at different initial vertical separation distances as shown in Fig. 14a, it can be seen that the trajectories approach an equilibrium solution in the vicinity of $\hat{\eta} = -0.9$, whereby the vertical shock velocity increases in absolute terms as the trajectories move away from the stationary point. Thus, this is a saddle point indicating the state of unstable shock-wave surfing. Interestingly, this relative vertical position of the saddle point matches to that of the sphere-wedge case in Laurence and Deiterding (2011) with a wedge angle of 10°. This similarity can be explained by the fact that the primary bow shock of the sphere is approximately equivalent to an oblique shock far downstream, which has roughly the same shock angle as that of the wedge. Thus, the positions of stationary points significantly depend on the shock angle.

For trailing cubes at different initial pitch angles as shown in Fig. 14b, there is a clear indication that a stable stationary point is located at low vertical shock distances close to zero

due to the appearance of bounding orbits. In doing so, the trailing cube with an initial setting of $\vartheta_{02} = -30^\circ$ (see cyan solid line in Fig. 14b) has a stable orbit in the phase plane for which the body follows the bow shock downstream without oscillations in the translational components as can be seen in Fig. 11a. From the present phase portrait, it is apparent once again that the initial pitch angle of the trailing cube at the same initial positioning is crucial for the separation behavior, since the phase paths tend to completely different directions. For example, both test cases at $\vartheta_{02} = -30^\circ$ and $\vartheta_{02} = 45^\circ$ with $\Delta\hat{x}_0 = 7.2$ indicate a saddle point at negative vertical shock distances, whereby the stationary point of the former seems to be further away from zero than of the latter.

By comparing the phase paths of the two body shapes, it can be seen that the cubes (see Fig. 14b) experience in general higher absolute vertical shock velocities unlike spheres (see Fig. 14a). The most interesting aspect of this comparison is that the trailing cube with $\vartheta_{02} = -30^\circ$ (see cyan solid line in Fig. 14b) experience stable shock-wave surfing in contrast to the sphere (see blue-gray solid line in Fig. 14a) with an unstable behavior, even though the initial points of the sphere trajectory are within the stable region of the cube’s phase path. This result suggests that non-spherical trailing bodies may have a larger region of stability that depends on their orientation. These findings might be explained by fact that the motion of trailing cubes is a result of both the body-inclination and the shock–shock interaction, which leads to mutual amplifications or attenuations of motion characteristics.

3.2 Wake–shock interaction

The following section discusses the impact of aerodynamic drafting during WSI of two axially aligned fragments for several different test cases with $\Delta\hat{x}_0 = 0.0$ (see test matrix in Table 4). Wake–shock interaction is of fundamental importance for our understanding of the impact footprints with respect to the crater depth due to the higher kinetic energy of drafting fragments. This section firstly presents results

Fig. 14 Phase diagrams of the trailing body’s motion behavior related to the leading sphere for different configurations at $\Delta\hat{x}_0 = 4.8$ (solid lines) and $\Delta\hat{x}_0 = 7.2$ (dashed lines): **a** spheres at various initial normalized vertical separation distances and **b**) cubes at various initial pitch angles

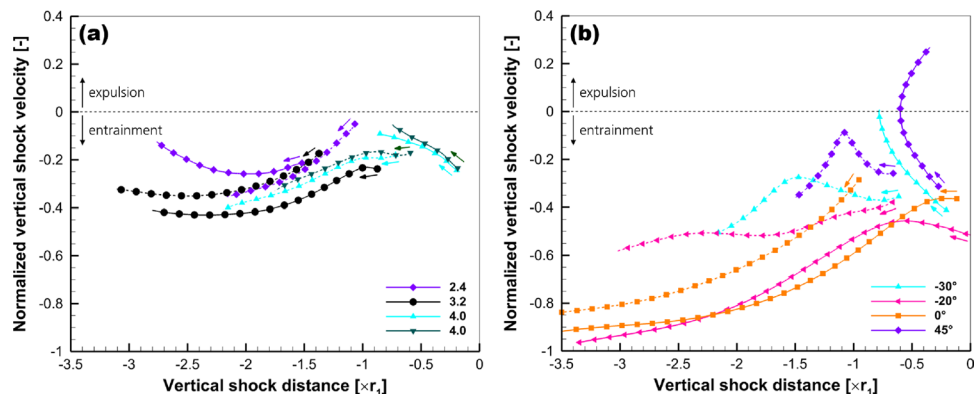
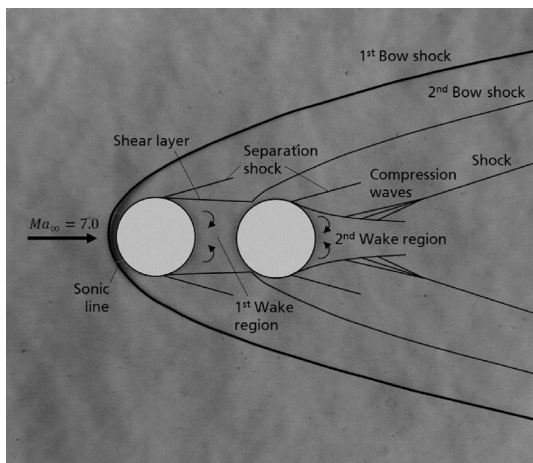


Table 4 Test matrix of WSI configurations

Primary shape	Secondary shape	ϑ_{01} (°)	ϑ_{02} (°)	$\Delta\hat{x}_0$ (-)
Sphere	Sphere	N/A	N/A	4.8
Sphere	Sphere	N/A	N/A	7.2
Sphere	Sphere	N/A	N/A	10.0
Sphere	Cube	N/A	+0	4.8
Sphere	Cube	N/A	+45	4.8
Sphere	Cube	N/A	+45	7.2
Cube	Cube	+45	+0	4.8
Cube	Cube	+45	+0	7.2

**Fig. 15** Qualitative flow field of a secondary sphere located in the near-wake of a primary sphere at $\Delta\hat{x} = 3.0$

concerning the flow structure, the motion behavior and aerodynamic coefficients of the front and aft object by way of example. The analysis of aerodynamic drafting will follow this part. Subsequently, the effect of body shape and inclination as well as the difference in the collision behavior is discussed, followed by the system dynamics of WSI.

3.2.1 Flow topology

In order to assess the impact of aerodynamic drafting, the key parameter in this subsection is the streamwise positioning with axial alignment of both bodies. Such a configuration is shown in Fig. 15 as a visualization of a stationary flow field with a schematic description of aerodynamic phenomena. The flow structures for the front half of the leading sphere are identical to the single-sphere topology as in Van Dyke (1982) until the point of boundary layer separation. Interestingly, the resulting wake region is bigger and narrows less downstream than of a single body. The reason for this is that the subsonic parts of the first wake region and the second stagnation region

merge into one another, so that the deflection of the flow occurs further upstream. Beyond the first wake region, the flow field is supersonic, which undergoes compression in front of the lateral areas of the trailing sphere by a usual bow shock that enables an outward flow deflection. However, this second bow shock is weaker in terms of the density gradient than the first one, since the total pressure ahead the shock is lower due to losses over the bow shock of the primary object. As can be seen from the schlieren representation, the bow shock of the trailing sphere originates from the end of the wake region's shear layer. Just like the single-body topology, the flow accelerates around the sides of the secondary sphere until the boundary layer separates, producing a typical wake flow.

Figure 16 displays three sequences of schlieren images with different combinations of spheres and cubes, whereby the time span between the first and last image of each sequence is 1/15 s. Each image depicts a different snapshot, with the first column showing the approach, the second column capturing the moment before the collision, and the third column showing the moment after. The exception to this is the pair of cubes (see Fig. 16c), which experience the first contact shortly before the second snapshot followed by a motion as coupled bodies. Regarding the flow structures, the characteristically detached bow shock of blunt bodies is apparent in Fig. 16, whereby the shock shape for cubes depends on their orientation angle relative to the inflow (Seltner et al. 2019). Furthermore, weak bow shocks ahead the trailing bodies as well as expansion fans and reattachment shocks on cube's leading edges can be seen in the schlieren images. This is contrary to the computations of Artemieva and Shuvalov (1996), which did not show a bow shock upstream the trailing body at a similar distance ($\Delta\hat{x} = 4.0$).

3.2.2 Model motions

An example for the measured displacement and its first derivative is provided in Fig. 17, whereby the translational (streamwise, spanwise and vertical) and angular (roll, pitch and yaw) components of the leading sphere and the trailing cube are presented over time. It is apparent from these charts that these both objects collide with each other 74 ms after the complete entering of the secondary model into the core flow. Until this moment, the results indicate a very good axial alignment during free flight with a maximum deviation in the separation distance of 2.1 mm in spanwise direction and of 2.0 mm in vertical direction. As in the SSI case (see Sect. 3.1.2), the out-of-plane motions prior to collision are substantially smaller than the corresponding in-plane motions and are therefore neglected in the subsequent analysis.

As can be seen from Fig. 17c and d, a collision causes sudden changes in the translational and angular velocities,

Fig. 16 Selection of schlieren image sequences showing the motion behavior in free-flight for different axially aligned body pairs: **a** sphere–sphere (S–S), **b** sphere–cube (S–C) at $\vartheta_{02} = 0^\circ$ as well as **c** cube–cube (C–C) at $\vartheta_{01} = 45^\circ$ and $\vartheta_{02} = 0^\circ$

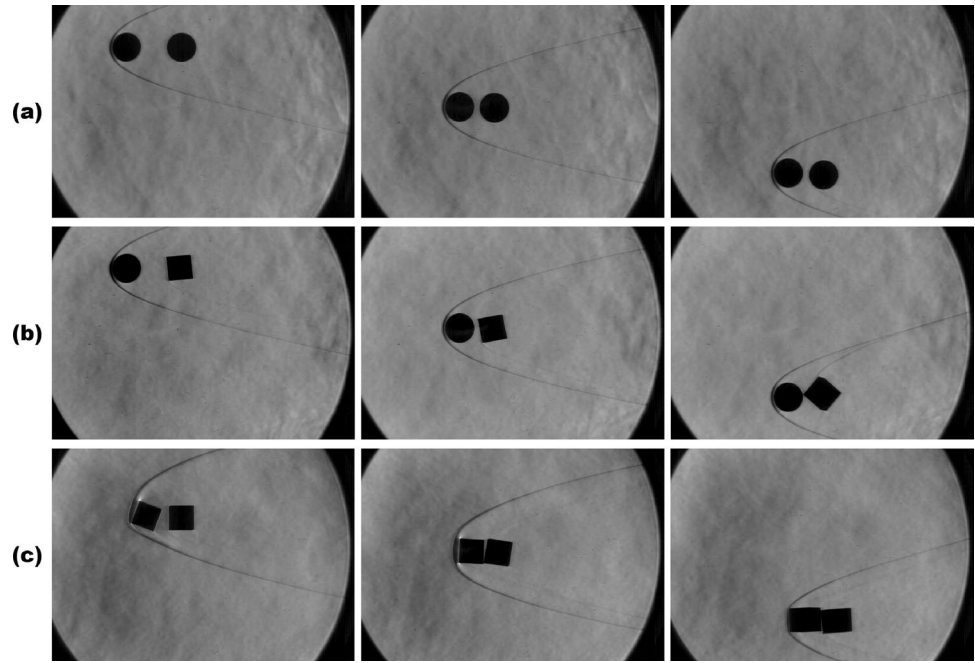
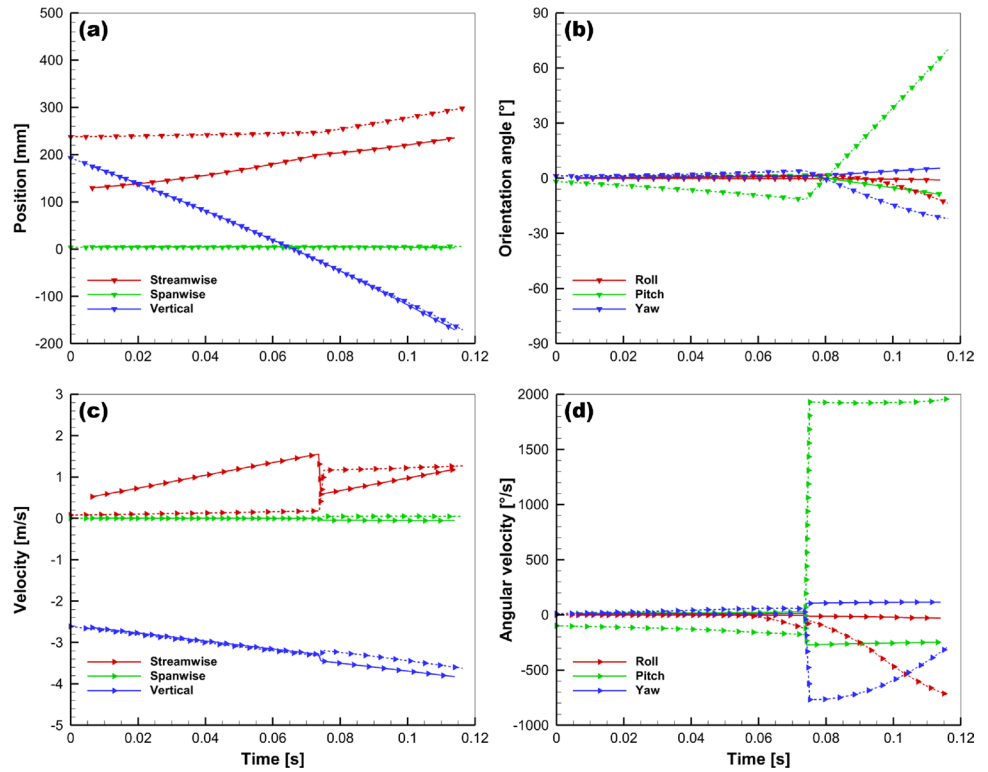


Fig. 17 Exemplary evolution of 6DoF translational and angular motion data in core flow of a leading sphere (solid lines) and a trailing cube (dashed lines) with $\Delta\hat{x}_0 = 4.8$ and $\vartheta_{02} = 0^\circ$: **a** positions, **b** orientation angles, **c** velocities and **d** angular velocities



particularly in pitch, yaw and streamwise direction. Small misalignments in combination with the impact lead to strong changes in all orientation angles, which are more pronounced for trailing cubes than for spheres. For this reason, the aerodynamic forces below are only shown for displacement data prior to a collision.

3.2.3 Aerodynamic forces

The resulting aerodynamic coefficients of an S–S configuration derived from the motion derivatives in streamwise (drag force) and vertical (lift force) direction are presented over the normalized time in Fig. 18. It can be seen that the

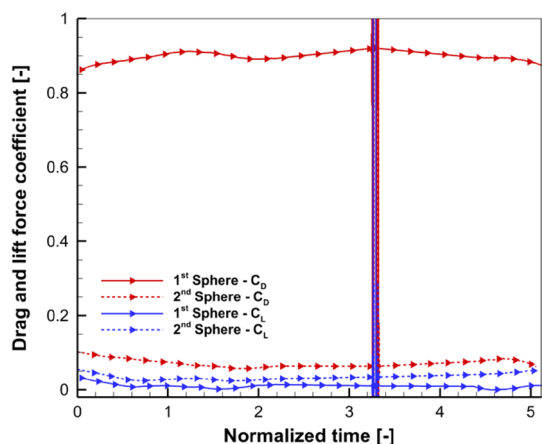


Fig. 18 Exemplary evolution of drag (red) and lift force coefficients (blue) in core flow of a primary (solid lines) and a secondary sphere (dashed lines) with $\Delta\hat{x}_0 = 4.8$

drag coefficient of the trailing sphere is 93.0% lower than that of the leading one with an average of $C_{D2} = 0.06$. The lift coefficients of both objects are close to zero, whereby the mean values for the entire time window in Fig. 18 are roughly 0.01 for C_{L1} and 0.03 for C_{L2} . Interestingly, this positive lift force of the secondary body is opposite to the negative vertical separation distance, since the vertical position of the aft body is slightly smaller than of the front one (see Fig. 16a). This result suggests that the primary wake region has a stabilizing effect on the trailing object. In addition, the extremely transient peak seen in each aerodynamic coefficient in Fig. 18 is an error in the data reduction due to the collision of the models.

3.2.4 Aerodynamic drafting

The term 'aerodynamic drafting' refers to a situation in which an axial alignment of objects reduces the drag of the downstream object and compressibility effects such as WSI dominate for supersonic flows. The reduction of the drag coefficient was previously demonstrated for a single test case in Fig. 18. This result is somewhat unexpected, since the effect of aerodynamic drafting is significantly lower in the hypersonic regime than in the subsonic one. Hoerner (1965) showed that the relative difference in drag coefficient between trailing and leading body is 134% for two equal cylinders in subsonic cross-flow with the same Reynolds number and the same relative distance as in the present study, which is significantly higher than for the two equal spheres at $Ma_\infty = 7.0$ in Fig. 18. The difference in the drag coefficient of the trailing body can be explained by the fact that wake–shock interaction leads to higher pressure loads on the windward surface and hence higher drag forces for hypersonic flow fields in contrast to subsonic ones.

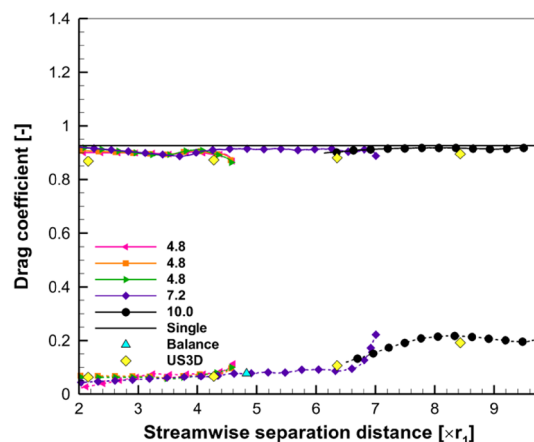


Fig. 19 Influence of streamwise separation distance on drag coefficient concerning leading (solid lines) and trailing sphere (dashed lines) for different initial streamwise positions

Figure 19 depicts the primary and secondary drag coefficients of several tests with different initial streamwise positions as a function of the streamwise separation distance. Please note that the first and also the last values of each dataset are partially influenced in the process of filtering by measurement points captured within the shear layer leading to slightly higher deviations at the edges of the graphs. From the chart, it can be seen that by far the trailing drag coefficient is strongly dependent on the streamwise separation distance. Its minimum with a median value of $C_{D2} = 0.05$ arises shortly before the contact of both spheres at $\Delta\hat{x} = 2.0$. By increasing the streamwise separation distance, the drag coefficient of the trailing sphere rises linearly until a transition point with a sharp increase and then remains nearly constant at approximately 0.20 within the observed range. It is apparent from Fig. 19 that the transition point is in the vicinity of $\Delta\hat{x} = 6.5$, but the exact distance cannot be determined due to significant deviations between different runs at this point. This transition could be attributed to the flow field of arrangements where the trailing body is affected by the compression waves and the shock originating from the primary wake region.

Turning now to the drag of the leading object, a weak upstream effect of WSI can be seen in Fig. 19, whereby its drag coefficient is on average 1.7% lower than the value of a single sphere with an overall uncertainty of 0.2% (Seltner et al. 2018). This finding is consistent with that of a previous study by Erengil et al. (1995) with hemispherical bodies. It can be seen that this difference decreases with higher separation distance in x -direction, whereby a minimum is apparent at $\Delta\hat{x} = 3.7$. The observed reduction of drag coefficient can be attributed to the subsonic wake region between both bodies as depicted in Sect. 3.2.1. In contrast to supersonic flows, the subsonic wake flow causes a pressure rise in upstream

direction due to the stagnation in front of the trailing object. As a result, the pressure on the leeward surface of the leading sphere increases, which results in a reduction of the overall drag force.

To demonstrate the accuracy of the present experimental results, high-quality data of force-balance measurements with a free-falling and a fix-mounted sphere were conducted as used by Willems et al. (2018). These tests were performed with spheres of $r = 0.05$ m at flow conditions reported in Sect. 2.1. The secondary drag coefficient for the same nominal distance of $\Delta\hat{x} = 4.8$ exhibits a very good agreement between both the stereo-tracking system and the force moment-type balance (see cyan triangle in Fig. 19) having a relative difference of 0.4%. In addition, the corresponding outcome of previous numerical simulations by using the viscous US3D solver is provided in Fig. 19 according to Venkatapathy et al. (2017). Although the data show a good agreement in general, the drag coefficients of the leading sphere are slightly underestimated by the numerical simulations compared to the experiments.

Figure 20 presents relative flight trajectories in the xz -plane of in-line S-S configurations with different initial streamwise distances. What stands out first is the occurrence of a relative vertical displacement in the beginning of all shown test cases. The reason why these slight separations have been emerged is that the free-flying objects experience a positive lift induced by the nozzle shear layer as already mentioned. In doing so, the trailing body is affected by a lower force due to the shielding by the leading one in the contrast to SSI configurations (see Sect. 3.1.4). However, it can also be seen that this separation approach quickly ends and the vertical separation distance stays constant until the collision. Thereupon, both spheres separate in streamwise as well as in vertical direction. The most important aspect

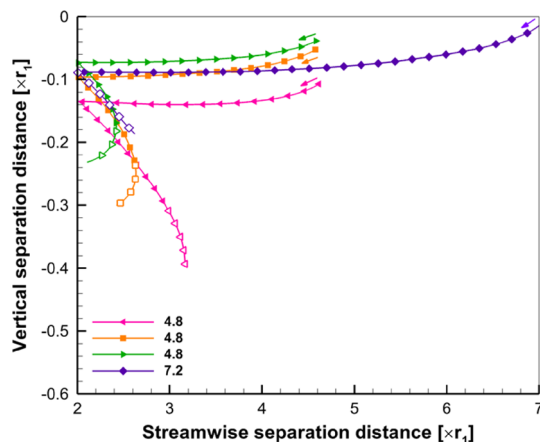


Fig. 20 Normalized flight trajectories of trailing related to leading spheres in core flow (closed symbols) and bottom shear layer (open symbols) for two different initial streamwise positions

of Fig. 20 is that in-line arrangements are mainly driven by a strong attraction of both bodies in streamwise direction, which results in the trailing objects remaining in the near-wake of their leading objects. However, the present experiments show that the trailing bodies undergo a slight lateral separation after collision, whereby they tend to be attracted again in streamwise and to slow down the separation in vertical direction. Due to the two occurring effects of aerodynamic drafting and collision, it is not possible to state with absolute certainty whether the trailing body of sphere–sphere configurations is expelled from the near-wake after the collision or remains in it as a final zone location according to Register et al. (2020).

3.2.5 Effect of body shape & inclination

A comparison of trailing object's outcomes with different body shapes, initial orientation angles and initial streamwise positions is depicted in Fig. 21 as a function of the streamwise separation distance to the leading sphere. Figures 21a and 21b show the drag coefficients based on a reference area with a constant base area S_{ref} and a pitch-angle-dependent projected frontal area $S_{ref,pro}$, respectively. The pitch angle is provided in Fig. 21c. From this figure, it can be seen that trailing cubes have a higher pitch velocity due to the shear layer (as outlined in Sect. 3.2.1) compared to spheres. In Fig. 21a, it is apparent that the drag coefficient of cubes is higher than of spheres and becomes even higher as the pitch angle changes from plane-exposed ($\vartheta = 0^\circ$) to more edge-exposed ($\vartheta = 45^\circ$) orientations. However, the differences in the trailing drag coefficient between the present configurations are reduced when the projected reference area is used (see in Fig. 21b). Interestingly, this finding is contrary to an earlier study with single cubes (Seltner et al. 2019), which depicts a strong influence of the pitch angle on the drag coefficient based on the projected reference area as well as a decrease in drag for more slender configurations as the edge-exposed cube. As a result, the main driver for the observed deviations in Fig. 21a for S-C configurations is the effective aerodynamic front face, while a slight influence of the geometry was found for the secondary drag coefficient by comparing spherical and cubical bodies. Interestingly, the relative difference between the drag coefficient of the trailing and the single body ranges from 90 to 95%, regardless of the body shape. Moreover, no significant influence on the transition point was identified between both geometries.

In these experiments, much higher absolute relative velocities were found in streamwise direction than in lateral direction as a result of the aforementioned aerodynamic drafting. Figure 22 provides the normalized streamwise separation velocity over time for different configurations. The results depict a roughly linear characteristic having their absolute peak at $\Delta\hat{v}_x = -1.56$, which is nearly twice as high

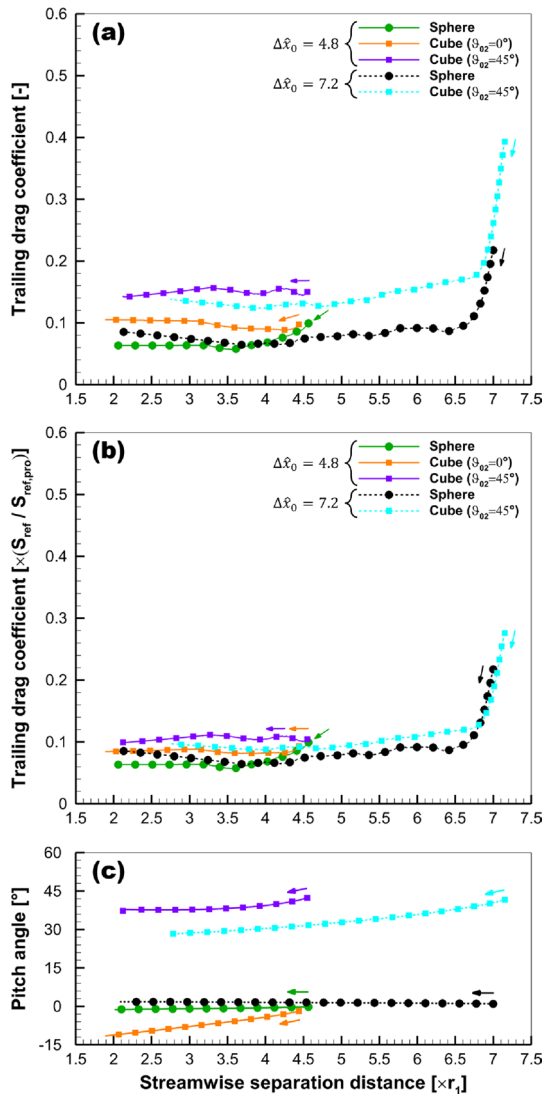


Fig. 21 Trailing drag coefficient as a function of the normalized streamwise separation distance based on **a** base reference area and **b** projected reference area in combination with **c** pitch angles for different configurations

as the maximum of the vertical component in SSI configurations (see Fig. 12). In Fig. 22, there is no evidence that either trailing body shape or orientation have a significant influence on the peak of streamwise separation velocity. By contrast, the geometry of the leading object has a strong effect on the peak streamwise separation velocity, while a good agreement of the collision time for different body shapes can be seen by using the normalized time. A much higher peak value and a steeper slope of the streamwise separation velocity in case of a leading cube compared to a sphere can be seen in Fig. 22, whose peaks differ by 20.0% based on the median value of the three tests with primary sphere. This finding is not surprising, because the ballistic coefficient of the cube is lower than of the sphere causing a

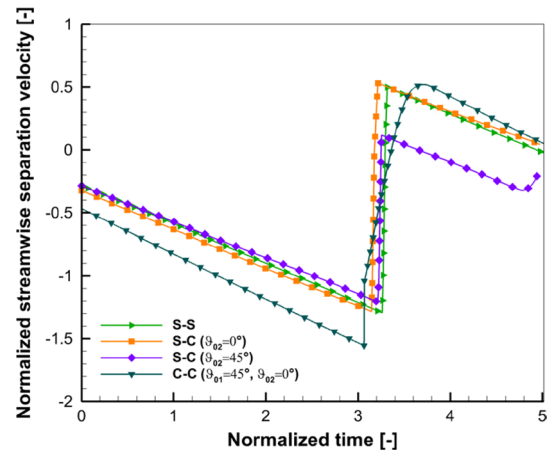


Fig. 22 Evolution of normalized streamwise separation velocity for different configurations at $\Delta \hat{x}_0 = 4.8$

larger acceleration in x -direction and hence a higher relative magnitude of the velocity.

3.2.6 Effect of collision

It is also of interest to discuss how the collision impacts the subsequent motion behavior as well as the final zone location of the secondary object, which has not been investigated in the literature before. Figure 23 shows the relative flight trajectories of the trailing body for different combinations of shape and orientation with the same initial distance of $\Delta \hat{x}_0 = 4.8$. In addition to the significant influence of the vertical separation distance mentioned earlier, it is apparent from this line chart that the motion behavior after impact also seems to depend strongly on the shape and orientation of both bodies. For example, a sphere (see green line in Fig. 23) moves in the opposite

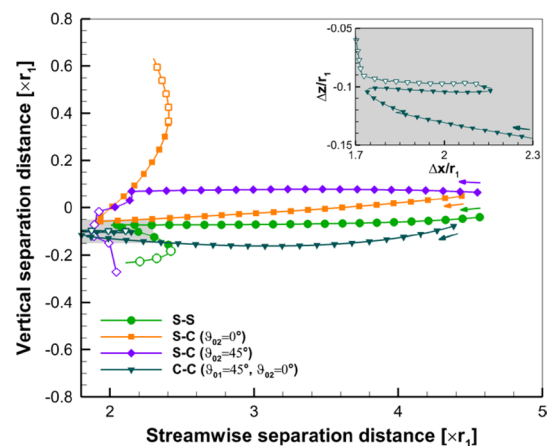


Fig. 23 Normalized flight trajectories of trailing related to leading bodies in core flow (closed symbols) and bottom shear layer (open symbols) for different configurations at $\Delta \hat{x}_0 = 4.8$ including an enlarged view of a single configuration in the top right corner

direction after a collision in contrast to a cube (see orange line in Fig. 23) in the case where they collide with a leading sphere at almost the same vertical separation distance. This finding can be explained by comparing the second schlieren image of Fig. 16a and b, where the sphere impacts the front body on the lower surface while the cube has the impact point on the upper surface. Surprisingly, although the final streamwise separation velocities of both trailing objects are roughly the same (see Fig. 22), the cube experiences a much stronger separation in lateral direction after the collision than the sphere. An interesting implication of this finding is that if the aft object continues to separate in lateral direction, it will be impinged by the primary bow shock. As a result, the trailing object ends in another final zone. This seems to be more likely for non-spherical bodies. Furthermore, multiple collisions can be seen in Fig. 23 for trailing cubes, which shows a coupling of both bodies with increasingly weaker impacts. In extreme case, both objects are coupled immediately without strong impacts (see blue-gray line in Fig. 23), which was also observed for this C–C configuration in Fig. 16c.

3.2.7 System dynamics

A phase-plane analysis was carried out to assess the stability behavior of the objects in the proximity of the primary wake region until the collision. Only the vertical motion component is considered, because no significant dependence of the streamwise distance on the lift force was found for in-line configurations. Thus, the system of differential equations is as follows:

$$\frac{d(\Delta\hat{z})}{d\hat{t}} = \Delta\hat{v}_z, \tag{10}$$

$$\frac{d(\Delta\hat{v}_z)}{d\hat{t}} = fC_L(\Delta\hat{z}), \tag{11}$$

where the shape factor f is 3/8 for spheres and 1/4 for cubes. It should be noted that the speed of the free-flying object is negligible compared to the free-stream velocity. Several phase paths of the trailing body’s motion are presented in Fig. 24 for different combinations of primary and secondary model. From this phase portrait, it is apparent that all system trajectories are neutrally stable for a variety of initial conditions in terms of axial distance, shape and orientation, indicating an attraction of the trailing object toward the primary wake region. A stationary point exists when the separation distance and velocity in z -direction are both zero. The state of the stationary point can also be assessed by determining the eigenvalues of the Jacobian matrix of Eqs. (10 – 11). As a linearized solution, the following eigenvalues are obtained:

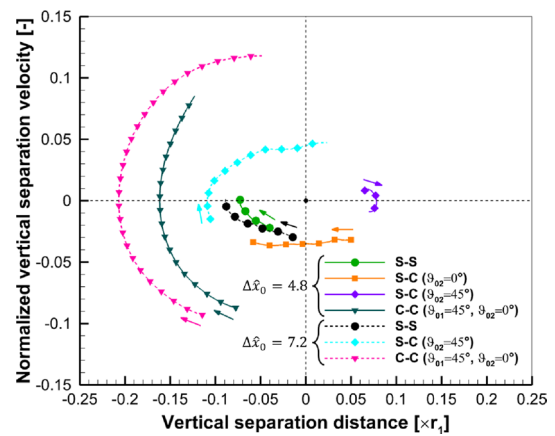


Fig. 24 Phase diagram of the trailing body’s motion behavior related to the leading object for different configurations at $\Delta\hat{x}_0 = 4.8$ (solid lines) and $\Delta\hat{x}_0 = 7.2$ (dashed lines)

$$\lambda = \pm \sqrt{f \frac{dC_L}{d(\Delta\hat{z})}} \tag{12}$$

At the stationary point, the gradient of lift coefficient is negative for both positive and negative vertical separation distances (see Fig. 10b). Thus, the eigenvalues are imaginary, and hence, the stationary point is a center. Consequently, the primary wake region is a statically stable trimmed position for trailing blunt objects with regard to the vertical direction, which is true for the present configurations regardless of the shape of the leading and trailing body. This finding provides the explanation for why the near-wake and far-wake are steady-state final zone locations without consideration of collisions as found by Register et al. (2020). Several factors from the flow field could elucidate this static stability. First, a decreasing total pressure behind the leading object from the bow shock to the center of the wake has the effect of a sink. Second, the high momentum of the wake’s shear layer, as shown by Erengil et al. (1995), acts like a barrier hampering the escape of the trailing object from the wake region. However, it can be assumed that the lift coefficient of trailing cubes in asymmetric flight attitudes is nonzero unlike spheres, because their lift coefficient also depends of the pitch angle. This implies that the stationary point is slightly shifted away from axially alignment in vertical direction, assuming a pitching moment of zero.

4 Conclusion

This study sets out to experimentally investigate the influence of body shape and inclination on the aerodynamic behavior of tandem-body configurations at Mach-7 with shock–shock interactions or wake–shock interactions.

Free-flight tests with sphere–sphere, sphere–cube and cube–cube arrangements were performed at the H2K test facility by the use of stereo-tracking measurement technique to determine the 6DoF motion data as well as schlieren videography to visualize the flow topology. Motion derivatives including aerodynamic coefficients were computed based on the time-resolved positions and orientation angles of the measurement data by means of a comprehensive post-processing, which considers a separate treatment of the signals concerning the singularity in the case of a collision.

Taken together, high-quality experimental data could be gained on the strong relationship between the lateral distance of two equal spheres and the aerodynamic force coefficients, as well as the streamwise distance between two axially aligned objects and the drag coefficient. Additional reference drag data of a balance measurement exhibit a very good agreement with the present motion data by stereo-tracking. For the configurations with shock–shock interactions, the results show that the sensitivity of the relative distance on the drag and lift coefficients is higher in lateral than in streamwise direction. Regarding the shape effect of the trailing body, it has become apparent that cubes experience significantly higher absolute drag and lift coefficients by a factor of 2 to 3 for tests with observed shock-wave surfing in contrast to spheres. As a result, the normalized final lateral velocities are mostly many times higher for cubical objects, which is due to two effects: shock–shock interaction and inclination-induced lift force. An implication of this inclination effect is that an additional factor is found, which explains in part the discrepancy between real-world observations and previous scientific studies. One of the more significant findings to emerge from this work is that the initial pitch angle of the trailing cube highly influences its entire flight trajectory and pitch orientation resulting in completely different separation behaviors. These experiments confirmed that the region of stable shock-wave surfing can be increased by means of a rotating trailing cube in comparison with a spherical object at the same initial conditions. The occurrence of this effect seems to depend on the initial flight attitude and direction of rotation. Furthermore, three simultaneous shock–shock interactions ahead the secondary object were observed in the schlieren images of cube–cube arrangements, which indicates the possible growth of the aerodynamic force coefficients compared to a leading sphere. During the experiments with wake–shock interactions, an attraction in flow direction of two axially aligned blunt bodies was observed, a phenomenon which is called aerodynamic drafting. Regardless of the shape and inclination of both objects, the secondary drag coefficient decreases by 90 to 95% relative to its single-body value. In terms of the absolute values, it was found that trailing cubes experience higher drag forces than spheres, whereby

higher pitch angle causes an increase in drag due to larger frontal area. The research has also shown that the leading object undergoes a slight reduction of drag due to a large subsonic region between both aligned objects. The most obvious finding to emerge from this study is that the primary wake region has a stabilizing effect on the relative lateral position of the trailing object. In this context, the stable trimmed position of the trailing object is in the vicinity of the primary wake's centerline. In contrast, collisions of both models with subsequent lateral separation of the trailing body were observed in some cases, with the motion depending on geometry and attitude.

A minor number of potential weak points of the present study need to be considered. First, the test matrix was not specially designed to observe shock-wave surfing for the cube–cube configurations, because the initial relative vertical distances between the objects were too short. Second, small lateral displacements between the centers of initially axial-aligned bodies arise before entering the core flow of H2K's free jet, which are the result of the different surface pressure distributions during the transition of the top shear layer. However, the impact of these slight displacements can be neglected, because the results show a very good agreement with reference data from a balance measurement of perfectly aligned objects. Third, the relationship of drag coefficient and streamwise separation distance is limited on measurement points within the near-wake, which is why the effect of higher distances in the far-wake is not investigated here.

A new focus on wake–shock interactions could produce interesting findings that give a comprehensive insight into the mechanisms of atmospheric (re)entry with breakups. Further studies regarding the impact of the body shape and inclination on the stable trimmed position in the primary wake region would be worthwhile. In addition, it would be important for future work to consider the pitch rotation in both directions with various angular velocities as well as elongated body shapes to understand how the likelihood of stable shock-wave surfing is influenced.

Acknowledgements This research was made possible by the DLR's program directorate *Defence & Security* as well as the PhD program *Helmholtz Research School on Security Technologies (HRSST)*. The authors wish to thank Mr. Michael Kosbow and Mr. Marco Schmors for their technical support in all our experimental work as well as Mr. Ansgar Marwege, Mr. Daniel Kirchheck, Mr. Dirk Allofs and Mr. Pawel Goldyn for our useful discussions. We also gratefully acknowledge the help provided by Mr. Eric Stern and the ATAP team, who gave us much valuable advice in the early stages of this work.

Author Contributions P.M.S. wrote the main manuscript text and prepared the figures. S.W. and A.G. discussed the results with P.M.S. All authors reviewed the manuscript.

Funding Open Access funding enabled and organized by Projekt DEAL. Open Access funding enabled and organized by Projekt DEAL.

Data availability Not applicable.

Declarations

Conflict of interest The authors declare that they have no conflict of interest.

Ethical approval Not applicable.

Open Access This article is licensed under a Creative Commons Attribution 4.0 International License, which permits use, sharing, adaptation, distribution and reproduction in any medium or format, as long as you give appropriate credit to the original author(s) and the source, provide a link to the Creative Commons licence, and indicate if changes were made. The images or other third party material in this article are included in the article's Creative Commons licence, unless indicated otherwise in a credit line to the material. If material is not included in the article's Creative Commons licence and your intended use is not permitted by statutory regulation or exceeds the permitted use, you will need to obtain permission directly from the copyright holder. To view a copy of this licence, visit <http://creativecommons.org/licenses/by/4.0/>.

References

- Artemieva NA, Shuvalov VV (1996) Interaction of shock waves during the passage of a disrupted meteoroid through the atmosphere. *Shock Waves* 5(6):359–367. <https://doi.org/10.1007/BF02434011>
- Artemieva NA, Shuvalov VV (2001) Motion of a fragmented meteoroid through the planetary atmosphere. *J Geophys Res: Planets* 106(E2):3297–3309. <https://doi.org/10.1029/2000JE001264>
- Barri NG (2010) Meteoroid fragments dynamics: collimation effect. *Sol Syst Res* 44(1):55–59. <https://doi.org/10.1134/S0038094610010077>
- Billig FS (1967) Shock-wave shapes around spherical-and cylindrical-nosed bodies. *J Spacecr Rocket* 4(6):822–823. <https://doi.org/10.2514/3.28969>
- Cardona V, Lago V (2022) Aerodynamic forces of interacting spheres representative of space debris re-entry: experiments in a supersonic rarefied wind-tunnel. *Acta Astronaut* 191:148–159. <https://doi.org/10.1016/j.actaastro.2021.10.036>
- Cardona V, Jousot R, Lago V (2021) Shock/shock interferences in a supersonic rarefied flow: experimental investigation. *Exp Fluids*. <https://doi.org/10.1007/s00348-021-03225-4>
- Daub D (2023) Experimental investigation of supersonic fluid-structure interaction for future space transportation systems. PhDthesis, DLR/RWTH Aachen University, Cologne/Aachen, DLR-FB 2023-09. <https://doi.org/10.57676/cbaa-ce26>
- Edney BE (1968) Anomalous heat transfer and pressure distributions on blunt bodies at hypersonic speeds in the presence of an impinging shock. Tech report FFA Report 115, The Aeronautical Research Institute of Sweden, Stockholm. <https://www.osti.gov/servlets/purl/4480948>
- Erengil ME, Reinecke WG, Dolling DS, Pike JA (1995) The aerodynamics of tandem bodies at Mach 5 - Part I: preliminary experimental results. In: 33rd Aerospace sciences meeting and exhibit, american institute of aeronautics and astronautics (AIAA), Reno, <https://doi.org/10.2514/6.1995-319>
- Hoerner SF (1965) Fluid-dynamic drag: practical information on aerodynamic drag and hydrodynamic resistance, 2nd Edn. Hoerner Fluid Dynamics, Bakersfield, California
- Kovács DG, Grossir G, Dimitriadis G, Chazot O (2023) Space debris interaction across a two-dimensional oblique shock wave. *Exp Fluids*. <https://doi.org/10.1007/s00348-023-03686-9>
- Laurence SJ, Deiterding R (2011) Shock-wave surfing. *J Fluid Mech* 676:396–431. <https://doi.org/10.1017/jfm.2011.57>
- Laurence SJ, Deiterding R, Hornung G (2007) Proximal bodies in hypersonic flow. *J Fluid Mech* 590:209–237. <https://doi.org/10.1017/s0022112007007987>
- Laurence SJ, Deiterding R, Hornung HG (2009) Tandem spheres in hypersonic flow. In: Hannemann K, Seiler F (eds) *Shock Waves*, Springer, Berlin, vol 1, pp 713–718, https://doi.org/10.1007/978-3-540-85168-4_115
- Laurence SJ, Parziale NJ, Deiterding R (2012) Dynamical separation of spherical bodies in supersonic flow. *J Fluid Mech* 713:159–182. <https://doi.org/10.1017/jfm.2012.453>
- Leiser D, Löhle S, Zander F, Buttsworth DR, Choudhury R, Fasoulas S (2022) Analysis of reentry and break-up forces from impulse facility experiments and numerical rebuilding. *J Spacecr Rocket* 59(4):1276–1288. <https://doi.org/10.2514/1.A35204>
- Lemieux P (1999) The instability of shear layers produced by curved shocks. PhD thesis, California Institute of Technology, Pasadena
- Li T, Sui J, Gong S, Wu C (2015) Dynamical separation of rigid bodies in supersonic flow. *Sci China Technol Sci* 58(12):2110–2121. <https://doi.org/10.1007/s11431-015-5966-1>
- Lukashenko VT, Maksimov FA (2020) On the separation of two meteoroid fragments of different shapes. *J Phys: Conf Series*. <https://doi.org/10.1088/1742-6596/1479/1/012132>
- Marwege A, Willems S, Gülhan A, Aftosmis MJ, Stern EC (2018) Superposition method for force estimations on bodies in supersonic and hypersonic flows. *J Spacecr Rocket* 55(5):1166–1180. <https://doi.org/10.2514/1.A34128>
- Niezgodka FJ (2001) Der Hyperschallwindkanal H2K des DLR in Köln-Porz (Stand 2000). Tech report, DLR, Köln. <https://elib.dlr.de/13874>
- Park C, Brown JD (2012) Fragmentation and spreading of a meteor-like object. *Astron J*. <https://doi.org/10.1088/0004-6256/144/6/184>
- Park SH, Park G (2020) Separation process of multi-spheres in hypersonic flow. *Adv Space Res* 65(1):392–406. <https://doi.org/10.1016/j.asr.2019.10.009>
- Park SH, Kim J, Choi I, Park G (2021) Experimental study of separation behavior of two bodies in hypersonic flow. *Acta Astronaut* 181:414–426. <https://doi.org/10.1016/j.actaastro.2021.01.037>
- Passey QR, Melosh HJ (1980) Effects of atmospheric breakup on crater field formation. *Icarus* 42(2):211–233. [https://doi.org/10.1016/0019-1035\(80\)90072-X](https://doi.org/10.1016/0019-1035(80)90072-X)
- Patel M, Navarro-Martinez S (2023) Heat transfer to proximal cylinders in hypersonic flow. *Phys Fluids*. <https://doi.org/10.1063/50137905>
- Prévèreaud Y (2014) Contribution à la modélisation de la rentrée atmosphérique des débris spatiaux. PhD thesis, Institut Supérieur de l'Aéronautique et de l'Espace, Toulouse
- Register PJ, Aftosmis MJ, Stern EC, Brock JM, Seltner PM, Willems S, Gülhan A, Mathias DL (2020) Interactions between asteroid fragments during atmospheric entry. *Icarus* 337(113468), <https://doi.org/10.1016/j.icarus.2019.113468>
- Schultz PH, Sugita S (1994) Penetration and escaping the atmosphere of Venus and Earth. 25th Lunar and Planetary Science Conference. Lunar and Planetary Institute (LPI), Houston, pp 1215–1216
- Seltner PM, Willems S, Gülhan A (2018) Experimental determination of aerodynamic coefficients of simple-shaped bodies free-flying in hypersonic flow. In: First International Conference on High-Speed Vehicle Science Technology (HiSST), Council of European Aerospace Societies (CEAS), Moscow

- Seltner PM, Willems S, Gülhan A (2019) Aerodynamic coefficients of free-flying cubes in hypersonic flowfield. *J Spacecr Rocket* 56(6):1725–1734. <https://doi.org/10.2514/1.a34345>
- Seltner PM, Willems S, Gülhan A, Stern EC, Brock JM, Aftosmis MJ (2021) Aerodynamics of inclined cylindrical bodies free-flying in a hypersonic flowfield. *Exp Fluids*. <https://doi.org/10.1007/s00348-021-03269-6>
- Taguema L (2017) Investigation of aerodynamic interactions between a free-flying and a balance-mounted object. Master's thesis, RWTH Aachen University. <https://elib.dlr.de/117074/>
- Van Dyke MD (1982) An album of fluid motion, 1st edn. Parabolic Press, Stanford
- Venkatapathy E, Gülhan A, Aftosmis MJ, Brock JM, Mathias D, Neeb D, Rodriguez D, Seltner PM, Stern EC, Willems S (2017) In pursuit of improving airburst and ground damage predictions: Recent advanced in multi-body aerodynamic testing and computational tools validation. In: Fifth Planetary Defense Conference (PDC), International Academy of Astronautics (IAA), Tokio, poster
- Whalen TJ, Laurence SJ (2021) Experiments on the separation of sphere clusters in hypersonic flow. *Exp Fluids*. <https://doi.org/10.1007/s00348-021-03157-z>
- Whalen TJ, Laurence SJ, Deiterding R (2020) A numerical investigation of clustered spheres separating in Mach 20 flow. In: AIAA Aviation 2020 Forum, American Institute of Aeronautics and Astronautics (AIAA). <https://doi.org/10.2514/6.2020-2970>
- Willems S, Seltner PM, Gülhan A (2018) New experimental results about ATD3 shock–shock interaction test case. Aerothermodynamics and design for demise (ATD3) Workshop, European Space Agency (ESA), Noordwijk
- Zhdan IA, Stulov VP, Stulov PV (2004) Aerodynamic interaction of two bodies in a supersonic flow. *Dokl Phys* 49(5):315–317. <https://doi.org/10.1134/1.1763624>
- Zhdan IA, Stulov VP, Stulov PV (2005) 3D configurations of broken body fragments in a supersonic flow. *Dokl Phys* 50(10):514–518. <https://doi.org/10.1134/1.2123300>
- Zhukov BG, Kurakin RO, Rozov SI, Sakharov VA, Beloborodii MV, Drobyshevski EM, Shibanova NY (2002) Synchronous EM launch of two bodies with double-barrel railgun and some peculiarities of their hypersonic flight in air. In: Fourth International Workshop on Magnetoplasma Aerodynamics, International Liaison Group on MHD Energy Conversion, Moscow
- Zhukov BG, Kurakin RO, Sakharov VA, Bobashev SV, Ponyaev SA, Reznikov BI, Rozov SI (2013) Synchronous acceleration of two millimeter-sized bodies up to hypersonic velocities in a multichannel railgun. *Tech Phys Lett* 39(12):1057–1059. <https://doi.org/10.1134/S1063785013120146>

Publisher's Note Springer Nature remains neutral with regard to jurisdictional claims in published maps and institutional affiliations.